Title:
Axial Elongation of Caudalized Human Pluripotent Stem Cell Organoids Mimics Neural Tube Development

Short title:
Axial Elongation of Human Neural Tube Organoids

One sentence summary:
Here, the authors introduce an organoid model for neural tube development that demonstrates robust Wnt-dependent axial elongation, epithelial compartmentalization, establishment of neural and mesodermal progenitor populations, and morphogenic responsiveness to changes in BMP signaling.

Authors:
A. R. G. Libby[1,2†], D. A. Joy[2,3†], N. H. Elder[1,2+], E. A. Bulger[1,2+], M. Z. Krakora[2], E. A. Gaylord[1], F. Mendoza-Camacho[2], T. C. McDevitt[2,4*]

Affiliations:
[1] Developmental and Stem Cell Biology PhD Program, University of California, San Francisco, CA
[2] Gladstone Institutes, San Francisco, CA
[3] UC Berkeley-UC San Francisco Graduate Program in Bioengineering, San Francisco, CA
[4] Department of Bioengineering and Therapeutic Sciences, University of California, San Francisco, CA
* Corresponding author: todd.mcdevitt@gladstone.ucsf.edu
[†] These authors contributed equally to this work.
[+] These authors contributed equally to this work.

Abstract:
During mammalian embryogenesis, axial elongation of the neural tube is critical for establishing the anterior-posterior body axis, but is difficult to interrogate directly because it occurs post-implantation. Here we report an organoid model of neural tube extension using human induced pluripotent stem cell (hiPSC) aggregates that recapitulates morphologic and gene expression patterns of neural tube development. Axial extending organoids consisted of longitudinally elongated epithelial compartments and contained TBXT(+)SOX2(+) neuromesodermal progenitors, PAX6(+) Nestin(+) neural progenitor populations, and MEOX1(+) paraxial mesoderm populations. Wnt agonism stimulated axial extensions in a dose-dependent manner and elongated organoids displayed regionalized rostral-caudal HOX gene expression, with hindbrain (HOXB1) expression distinct from brachial (HOXC6) and thoracic (HOXB9) expression. Finally, CRISPR interference-mediated silencing of BMP inhibitors induced elongation phenotypes that mimicked murine knockout models. These results indicate the potent morphogenic capacity of hiPSC organoids to undergo significant axial elongation in a manner that mimics early human nervous system development.

Main Text:
Introduction

Proper development of multicellular organisms depends on the regulated emergence and coordinated organization of multiple cell types to form tissue structures and organs. An essential example of such morphogenesis is the creation and extension of the neural tube, which eventually forms the spinal cord. Defects in this process result in severe congenital abnormalities (1), highlighting the clinical importance of understanding human spinal cord development. However, many of the molecular mechanisms and cellular behaviors that regulate formation of the central nervous system remain unknown because neural tube morphogenesis is a dynamic process that occurs post-implantation (2, 3).

Formation of the central nervous system in amniotes begins at gastrulation, when neuroectodermal progenitors establish the anterior neural plate. This structure folds to form the anterior neural tube, which will ultimately become the brain and cervical spinal cord. By contrast, the remainder of the spinal cord is generated from a separate pool of neuromesodermal progenitors (NMPs), that reside at the node-streak border and caudal-lateral epiblast immediately post-gastrulation, and in the chordoneural hinge of the tail bud later in development (2, 4-6). NMPs are bipotent progenitors that contribute to the developing neural tube and the surrounding paraxial mesoderm, facilitating extension of the embryo along the anterior-posterior body axis. The

subsequent differentiation, patterning, and development of the multiple cell types within the elongating neural tube relies on a series of overlapping morphogen gradients that extend along both the anterior-posterior and the dorsal-ventral axes of the embryo. The anterior-posterior axis of the neural tube is patterned by the Wingless-type MMTV integration site family (Wnts), the fibroblast growth factors (FGFs) produced from the tailbud, and retinoic acid (RA) released from the adjacent somites, which regulate progenitor proliferation and convergent extension (7-9). Dorsal-ventral patterning of the neural tube is dictated by opposing gradients of Sonic hedgehog (Shh) released ventrally from the notochord and floor plate, and bone morphogenic proteins (BMPs) released from the roof plate (10-12).

The development of differentiation protocols for pluripotent stem cells has revealed key factors, particularly morphogen combinations, regulating the emergence of neuronal populations in the developing spinal cord. These advances have enabled robust production of neuronal subtypes *in vitro* (13, 14). In parallel, organoid models capable of recapitulating structures reminiscent of early embryonic tissue have been developed as tangible platforms for disease modeling, drug testing, and mechanistic study of development (15). More specifically, organoids displaying axonal extensions through neuromuscular junctions (16), mimicking spinal cord elongation through budding extensions of NMPs (17), or 3D gastruloid elongation (18) have extended the ability of *in vitro* systems to study developmental morphogenesis. However, to date, no organoid model exhibits both extensive unidirectional elongation and emergence of tube-like structures mirroring the endogenous cell behaviors that contribute to human spinal cord morphogenesis. Here we report the development of an organoid model of axial extension derived from human induced pluripotent stem cells (hiPSCs) that recapitulates the uni-axial elongation and morphogenesis of the neural tube in addition to regionalized gene expression profiles of spinal cord development. This model enables the direct examination of features of early human spinal cord development and patterning.

Emergence of Axial Extensions from Neuronal Organoids

In order to model early spinal cord development, we modified a previously described neuronal differentiation protocol (13) for generating hindbrain-level interneurons, with the goal of yielding caudalized neural populations. Organoids were formed by seeding singly-dissociated cells into non-adherent pyramidal inverted wells (10,000 cells/well) and allowed to aggregate for 18-24 hours before being transferred to rotary suspension culture in either 6-well plates or 10cm dishes **(Fig. 1A)**. To caudalize the cells from hindbrain to spinal cord identity (19), we added the small-molecule Wnt agonist CHIR99021 at a concentration of 2μM starting two days prior to aggregation and continuing through day 7 of differentiation **(Fig. 1B).** After 3-5 days in suspension culture, pronounced singular extensions emerged from the organoid bodies **(Fig. 1C)**.

Elongated organoids appeared to be continuous, with linear striations extending longitudinally from a central, more radially symmetric anterior aggregate body **(Fig. 1D)**. To confirm that elongation did not result from the fusion of multiple organoids during suspension culture, individual organoids from 10cm dishes were transferred into single wells of low-adherent, 96-well plates after 5 days of differentiation, and subsequently imaged for 48 hours, during the time period when extension appeared to be most robust. Approximately 70% of organoids grown in 10cm dishes, and 85% of organoids transferred to 96-well plates demonstrated at least partial elongation **(Fig. 1E, S1A, B)**. Extending organoids doubled the ratio of their longest axis relative to their shortest axis, whereas the length of the shortest axis did not differ between non-extending and extending organoids **(Fig. 1E, Fig. S1C, Movie S1-2)**. Additionally, extending and non-extending organoids displayed several quantifiable morphometric differences **(Fig. 1E, Fig. S1C)**. Time lapse microscopy definitively demonstrated that axial elongation of caudalized neural organoids results from autonomous symmetry-breaking that is comparable to axial elongation observed in model organisms**.**

In follow-up studies, extensions were found to occur for organoids of various sizes (500, 3,000, or 10,000 cells at seeding) and continued to grow until day 10 of culture. However, the degree of extension varied depending on culture conditions. To determine if culture density affected the efficiency of extension, we varied the number of 3,000-cell organoids cultured in a fixed 2 mL volume, culturing aggregates at 68, 135, or 270 organoids per mL in suspension **(Fig. S2)**. While extension occurred in all conditions, extensions were more frequent and became more pronounced as organoid density decreased; however, at the highest density, elongation morphology was lost by day 15. Density-dependent effects were also observed when we cultured a fixed number of 10,000-cell organoids (270) in low (2 mL) or high (12 mL) media volumes, resulting in densities of 135 or 23 organoids per mL. Robustly elongating organoids formed when cultured at low density, whereas organoids failed to elongate when an equivalent number of organoids were cultured at high density **(Fig. S3)**.

In the lowest density condition (23 organoids per mL), extensions persisted through day 15 **(Fig. 1C)**, suggesting that density-mediated signaling parameters, such as paracrine effects or nutrient deprivation, play a role in inducing and maintaining axial extensions.

After analyzing the gross morphology , we examined the structural and gene expression differences between elongating and non-elongating organoids. Histological analysis of extending organoids revealed multiple internal elongated epithelial compartments separated by regions devoid of cells **(Fig. 1F, Fig. S4).** By comparison, non-extending organoids consisted only of small rosette structures distributed radially throughout the interior. To investigate whether structural differences were associated with distinct spinal progenitor populations, we performed quantitative PCR (qPCR) to identify changes in neural and mesodermal expression patterns. Both extending and non-extending organoids expressed neural progenitor markers such as SOX2, PAX6, HB9, and NeuN by day 17 of differentiation, however the levels of SOX2, HB9, and NeuN were greater in extending aggregates at that timepoint **(Fig. 1G)**. In addition to genes expressed in the early neural plate and neural tube (SOX2 and PAX6), Brachyury (TBXT), associated with primitive streak and mesoderm differentiation, was expressed in all organoids. However, NKX1.2, associated with embryonic axial extension, was expressed for a longer duration and at higher levels in elongating organoids **(Fig. 1G)**. The expression of NKX1.2, SOX2, and TBXT within organoids raised the possibility that NMPs and paraxial mesoderm present within organoids might account for the observed morphogenic phenomena.

Extending Organoids Display Polarization and Region Patterning

We next sought to understand how differences in the identity and spatial distribution of the cell populations in extending and non-extending organoids contributed to differential organoid morphologies. We first performed immunostaining of histological sections to investigate the cellular composition of extending organoids in relation to observed TBXT expression. At day 6, after the start of extension, organoids contained regions of co-localized SOX2 and TBXT expression **(Fig. 2A, white arrows)**, indicative of NMPs, while the surrounding cells expressed Nestin, a marker of neural commitment **(Fig. 2A)**. To more comprehensively visualize the location of TBXT(+) cells in 3D, we imaged extending and non-extending organoids via light-sheet microscopy at day 7 of differentiation. In extending organoids, TBXT(+) cells were localized within the extensions, whereas in non-extending organoids TBXT(+) cells were dispersed around the edges of the organoid body **(Fig. 2B, Movies S3-4).** In most extending organoids, the TBXT(+) populations formed a streak lining the extension, analogous to the morphology of the notochord, and accumulated at the end of the extension **(Fig. S5A)**. In addition, extending organoids contained a higher percentage of TBXT(+) cells **(Fig. S5B)**. Interestingly, staining in organoids at day 3 (before extension occurred) revealed distinct sorting patterns of either radially symmetrical populations of TBXT(+) cells or polarized clustering of TBXT(+) cells within the organoids **(Fig. S6).** Both extending and non-extending organoids contained cells expressing the neuronal progenitor marker Nestin and β3-tubulin at day 10 of differentiation, indicating that the majority of cells differentiated to a neural fate **(Fig. 2B, Fig. S7, Movies S5-6)**. However, in the extending organoids, the neural-committed cells organized into distinct compartmentalized layers surrounding lumens within the extensions.

To further interrogate the distinct striations observed by brightfield microscopy and the inner epithelial layers seen in histology, we examined cell polarity by staining for collagen IV (COL IV), a marker of the basement membrane, and zona occluden-1 (ZO-1), a marker of tight junctions at cellular apical domains. An increase in basement membrane deposition and polarized cells was observed between days 7 and 10 of differentiation in extending organoids **(Fig. S8)**. After 10 days, ZO-1 was apparent at the apical domain of cells in the outer epithelial layers of the extensions, as well as in cells facing inward toward the internal lumens **(Fig. S8,9)**. Distinct layers of basement membrane marked by collagen IV were observed basally to ZO1, forming a bilayer between lumens and organoid exterior **(Fig. 2B, Fig. S8,9. Movies S7-8)**. Bilayers of cells were also apparent in non-extending organoids **(Fig. S9)**, but to a lesser extent since the internal lumens were much smaller.

In order to ascertain whether extensions resulted from a polarized population of proliferative cells, we examined EdU incorporation on days 6, 7 and 9 of differentiation **(Fig. 2C)**. A two-hour EdU pulse labeled over 50% of cells in extending organoids, but proliferation was not spatially restricted, indicating that proliferation of cells throughout organoids contributed to their growth. To examine transcriptional differences between the two poles of extending organoids, we manually dissected the “anterior”, or main organoid body from the “posterior”, or extending portion of day 9 extending organoids and performed comparative qPCR **(Fig. 2D, Fig. S10)**.

Expression of hindbrain Hox genes (HOXA2, HOXB4) was enriched in the anterior portion of the organoids. Correspondingly, the posterior regions had increased expression of more caudal HOX genes, particularly HOXB9 and HOXC10, associated with the thoracic and lumbar regions of the spine, respectively (9, 20). The posterior extending regions also expressed higher levels of transcripts associated with caudalization and the tail bud, such as CDX2, FGF8, HES7 and TBXT, indicating that the extending regions of the organoids had a more caudal fate specification than the anterior. The posterior extending portions of the organoids also displayed increased expression of ALDH1A2, indicating an increase in retinoic acid signaling, potentially from TBXT (+) mesoderm.

To determine how well extension morphology and localized HOX gene expression mimicked the regionalization of the spinal cord, we examined HOX gene transcripts marking hindbrain (HOXB1), brachial (HOXC6), and thoracic (HOXB9) regions of the neural tube via RNAscope in day 7 and day 10 organoids **(Fig. 2E,F)**. While non-extending organoids expressed both hindbrain and brachial HOX genes, the expression was distributed radially, and the expression of HOXB9 was delayed relative to extending organoids. In contrast, extending organoids displayed regionalized expression of hindbrain, brachial and thoracic HOX genes along the axis of extension, as seen in the neural tube of developing vertebrates. Specifically, we observed enrichment of HOXB1 (hindbrain) in the central mass of the organoid, and HOXC6 (brachial) and HOXB9 (thoracic) in the extensions **(Fig. 2E)**. Interestingly, HOXC6 and HOXB9 often overlapped at day 7 within extending organoids **(Fig. 2E)**, however by day 10 HOXB9 was more pronounced than HOXC6 in the extension regions, suggesting a transition to a more posterior fate. Although non-extending organoids expressed multiple HOX genes, regionalized expression was infrequently detected and non-extending organoids did not express detectable HOXB9 levels until day 10 **(Fig. 2F).** These data indicate that while organoid extension is not a requirement for posterior HOX expression, extension enables the stratification of distinct HOX domains. Overall, extending and non-extending organoids maintained similar HOX profiles, but the cell behaviors that contribute to symmetry breaking and subsequent elongation, perhaps through the establishment and maintenance of an NMP pool, allowed for HOX domain segregation similar to that observed in neural tube development.

Wnt Pathway Activation Increases Extension Formation and SOX2(+)TBXT(+) Progenitors

Caudalization of the spinal cord (21) and differentiation of NMPs (2, 22) are critically dependent on Wnt signaling. Therefore, we assessed how increasing canonical Wnt signaling impacted organoid elongation. Escalating doses of CHIR (2μM, 4μM, and 6μM) enhanced the length of extending organoids **(Figure 3A,B)**, and increased the ratio of longest:shortest radial axis in response to Wnt early in the differentiation **(Fig. 3C,D, Fig. S11A)**. Initially, differentiation studies were conducted with a commonly used male hiPSC line (WTC) (23, 24). In contrast, organoids created with a female hiPSC cell line (WTB) failed to elongate in the presence of 2μM CHIR, but did respond to increasing doses of WNT activation **(Fig. 3D, Fig. S11B)**, though not to the same extent as WTC-derived organoids. At later timepoints, aggregates in both cell lines and at all but the highest CHIR dose become more round, suggesting that early polarized extension succumbs to later radial expansion. Overall, the variation in extension length between cell lines implies that inherent differences between hiPSC genomes may influence an organoid's capacity for axial extension, similar to previously reported differences between various human pluripotent stem cell lines (25, 26).

At day 10 of differentiation, histological sections of extending WTC-derived organoids treated with 4μM- and 6μM-CHIR revealed cells that co-expressed SOX2 and TBXT, with an increasing number of TBXT(+) cells as Wnt signaling agonist was increased **(Fig 3E,F)**. Additionally, TBXT(+) cells were typically surrounded by a bilayer of TBXT(-) cells **(Fig. 3E).** Organoids exposed to 4μM- and 6μM-CHIR expressed SOX2 and PAX6 in distinct regions of the organoids, whereas organoids exposed to 2μM CHIR displayed SOX2 and PAX6 expression throughout, suggesting a loss of neural progenitor states or a non-neuronal population in higher Wnt signaling environments. All organoids displayed N-cadherin and βIII-Tubulin expression, indicating the emergence of more mature populations of neurons; however, regions without N-cadherin or βIII-Tubulin were observed more frequently in organoids exposed to higher doses of CHIR, suggesting a Wnt-dependent reduction in the overall neural population **(Fig. 3E)**. Overall, increased stimulation of the Wnt pathway increased the NMP progenitor pool, facilitated progenitor maturation, and augmented organoid extension.

Similar Transcriptional Profiles within Extending and Non-extending Organoids

In order to identify the cell diversity within extending organoids and the differences between organoids that did and did not extend, we performed single-cell transcriptomics at day 10 of differentiation. In order directly compare elongating and non-elongating organoids under nearly identical conditions, differentiation was conducted under the original conditions with 2μM CHIR. Shared nearest neighbor computation revealed six clusters containing roughly equivalent percentages of cells from extending and non-extending organoids, with the exception of cluster 2, which contained a majority of cells from non-extending organoids **(Fig. 4A,B)**. Gene ontology (GO) terms for each cluster revealed similar biological processes, related largely to pattern specification and hind limb morphogenesis **(Fig. 4C)**. Neural markers such as SOX2 and Nestin were expressed in all clusters **(Fig. 4D,E)**, however, clusters 0 and 1 had higher expression levels of genes associated with early neural progenitors such as SOX2, PAX6 and NEUROG2 **(Fig. 4D, Fig. S12A)**. Clusters 0 and 1 contained cells with high expression of transcription factors and morphogens associated with the caudal lateral epiblast (CDX2, NKX1.2 and FGF8) **(Fig. 4D,E)**. In contrast, MIXL1, MEOX1, CYP1B1, MEOX2, and PAX3 were almost exclusively expressed in clusters 2-3, suggesting that these clusters contained mesodermal cells **(Fig. 4D,E, Fig. S12A)**. We did not observe expression of markers associated with the endodermal germ lineage such as SOX17, and observed only very low expression of FOXA1 and PAX9 in <1% of cells **(Fig. 4E),** indicating that both the non-extending and extending organoids consisted entirely of neural and mesodermal cell types, but not endoderm, in contrast to previously reported gastruloid models (18, 36). Further, no single cell cluster expressed genes associated with the developing notochord **(Fig S12B)**, however, single cell transcriptomic data did recapitulate HOX gene expression patterns within organoids **(Fig. 4F)**. Extending and non-extending organoids both expressed genes associated with the hindbrain and the brachial and thoracic regions of the neural tube, but only a minor increase in HOX gene expression was detected in extending relative to non-extending organoids (average 1.3-fold change), which was in agreement with our RNAScope analysis. Overall, these gene expression results indicate similar cell specification within non-extending and extending organoids, suggesting that post-transcriptional regulation or morphogenic differences account for the distinct organoid phenotypes.

Manipulation of Endogenous BMP Signaling Influences Dorsalization and Degree of Extension

BMP signaling is critical to establish both the anterior-posterior Wnt and FGF gradients that drive axial elongation, and the BMP-SHH dorsal-ventral gradient that organizes the developing spinal cord (8, 17, 21, 27). In vertebrate development, Noggin is expressed along the developing neural tube and inhibits dorsally expressed BMP. Noggin deletion in murine models leads to increased BMP signaling at the posterior axis, failure of neural tube closure, and elongation of the developing tail (27). Chordin is a BMP shuttling molecule that concentrates BMP at the dorsal side of the neural tube; in mice, deletion of Chordin results in a shortened body axis and underdeveloped anterior spine (28). Therefore, we assessed the role of endogenous BMP signaling in extending organoids by knocking down (KD) Noggin and Chordin. We introduced RNA guides targeting Noggin and Chordin into a Lamin-B GFP labeled WTC hiPSC line harboring a doxycycline (DOX) inducible CRISPR interference system (CRISPRi) (29, 30), and supplemented the media with DOX at the start of differentiation **(Fig. 5A).** Noggin and Chordin gene expression significantly decreased 5 days after the addition of DOX **(Fig. 5B)**. Both Chordin and Noggin KD resulted in increased extension compared to wildtype organoids **(Fig 5C,D)**. However, the timing of extension differed, with Chordin KD organoids expanding rapidly within the first 7 days of differentiation then becoming more circular after day 10, while Noggin KD extended continuously, becoming more polarized through day 13 relative to WT organoids. The pronounced extensions in Noggin KD organoids appear analogous to Noggin knockout mice that develop elongated tails. In contrast, Chordin KD organoids initially developed blebs without clear anterior-posterior axis identity, and these disordered, kinked outgrowths were sustained through approximately day 11, similar to the shortened body axis characteristic of Chordin knockout mice.

In addition to contrasting the morphological phenotypes of different organoids, the relative proportions of dorsal-ventral markers of spinal cord progenitor neuron populations were assessed by qPCR at day 17 of differentiation. Expression of LIM Homeobox Protein 2 (LHX2), a marker of dI1 dorsal interneurons, did not significantly change under knockdown conditions. However, expression of LIM Homeobox Protein 5 (LHX5), a marker of V0 ventral interneuron populations, significantly increased under both Noggin and Chordin knockdown conditions **(Fig. 5E,F).** Expression of Engrailed1 (EN1), a marker of V1 interneuron progenitors, was increased in knockdown populations, while CHX10, a marker of V2a interneurons, and OLIG2, a marker of motor neurons, were unaffected. Attenuation of BMP inhibition would be expected to increase dorsal neural

populations, and these data indicate neural progenitors in Chordin and Noggin knockdown lines have a propensity to express more dorsalized markers relative to wildtype. Finally, we assayed markers of neural maturation and its regulation, including Sox2, Pax6, and Hes1. Hes1, which maintains neural progenitors in their immature state, was not significantly upregulated in the Chordin knockdown, nor were the neural progenitor markers Sox2 or Pax6. Altogether these results indicate that BMP signaling impacts the anterior-posterior morphology of the extending organoids in a manner that is similar to neural tube development *in vivo.*

Discussion

Here, we demonstrate that hiPSC-derived organoids can model axial extension via the specification of progenitors that dictate axial elongation and neural tube formation. Our model allows for robust axial extension as a function of both culture density and Wnt signaling, where either reduced organoid density or increased small molecule Wnt agonism promote elongation phenotypes and increased proportion of TBXT(+) cells. Within extending organoids, we observed a persistent NMP population and TBXT(+) streak along the extension of the organoid axis, reminiscent of similar phenotypic populations present in the caudal lateral epiblast, notochord, and later in the tail bud during axial elongation. Although both extending and non-extending organoids contained cells expressing cervical through thoracic HOX gene profiles, only extending organoids displayed regionalized co-linear patterning of HOX genes, and the timing of HOX gene expression differed between extending and non-extending populations. Single-cell RNA sequencing confirmed similar transcriptomic profiles with slightly differing levels of HOX gene expression between extending and non-extending populations, and also revealed that all organoids contain populations of neuronal progenitors and paraxial mesoderm. Significantly, this shows that despite similar gene profiles, morphological variation may occur due to differential regulation at the protein level. Finally, we demonstrated that the axial extension of organoids is influenced by BMP signaling, such that perturbation of endogenous BMP signaling via KD of inhibitors influences relative expression of neuronal markers along the dorsal-ventral axis. Noggin knockdown resulted in elongation that surpassed that of the wildtype control, mirroring Noggin knockout murine models that exhibit failed neural tube closure and elongated tails. Further, knockdown of Chordin expression yielded organoids that extended quickly in multiple directions, failing to create a uni-directional extension axis, which may be reminiscent of Chordin-deficient mice that have a shortened body axis (28). Overall, the organoid model described herein provides a novel approach to study the gene regulatory networks, multicellular organization, and structural outcomes that contribute to the development of the primitive human central nervous system.

Stem cell-derived organoid model systems that reflect multiple organ systems (16, 31-34) and stages of development (18, 35, 36) can now be used to investigate aspects of human embryogenesis that were previously elusive due to low quantity of tissue, technical difficulties isolating and imaging embryonic tissues, and ethical concerns regarding tissue procurement. Organoid platforms are amenable to varying culture conditions, genetically modified cell lines, or small molecule drug screens, enabling the systematic manipulation of experimental conditions in a higher throughput manner than possible in most model organisms. However, while substantial insights can be garnered from organoids, they do not perfectly recapitulate the spatiotemporal dynamics of gene expression and differentiation that occurs within an embryo (37). Additionally, reproducibility both within differentiations, between cell lines, and across labs remains a large hurdle. Therefore, refining organoid culture protocols and developing new differentiation systems to better reflect developmental conditions is crucial for understanding complex morphological processes that transpire uniquely during embryogenesis, such as axial elongation. Furthermore, refining tractable and manipulatable organoids that mimic embryonic morphogenesis will help to elucidate mechanisms that govern form and function, advancing the field of human developmental biology and enabling the discovery of new therapeutic interventions for congenital defects.

Materials and Methods

Human Induced Pluripotent Stem Cell Line Generation and Culture

All work with human induced pluripotent stem cells (iPSCs) was approved by the University of California, San Francisco Human Gamete, Embryo, and Stem Cell Research (GESCR) Committee. Human iPSC lines were derived from the WTC11 line (Coriell Cat. #GM25256), the WTB line (Conklin Lab)(38), and the Allen Institute WTC11-LaminB cell line (AICS-0013 cl.210). All cell lines were karyotyped by Cell Line Genetics and reported to be karyotypically normal. Additionally, all cell lines tested negative for mycoplasma using a MycoAlert Mycoplasma Detection Kit (Lonza).

Human iPSCs were cultured on growth factor reduced Matrigel (Corning Life Sciences) and fed daily with mTeSR^{TM}-1 medium (STEMCELL Technologies)(39). Cells were passaged by dissociation with Accutase (STEM CELL Technologies) and re-seeded in mTeSR^{TM}-1 medium supplemented with the small molecule Rho-associated coiled-coil kinase (ROCK) inhibitor Y-276932 (10 μM; Selleckchem)(40) at a seeding density of 12,000 cell per cm^2.

The generation of the Chordin and Noggin CRISPRi lines first involved TALEN mediated insertion of the CRIPSRi cassette pAAVS1-NDi-CRISPRi (Gen2) (Addgene) to the AAVS1 locus of the Allen Institute WTC11-LaminB cell line. Following antibiotic selection of clones that received the CRIPSRi cassette, CRISPRi gRNAs were generated targeting Noggin and Chordin (Table S2) using the Broad Institute GPP Web Portal and cloned into the gRNA-CKB (Addgene) following the previously described protocol (30). Guide RNA vectors were nucleofected into the LaminB CRISPRi iPSC line using a P3 Primary Cell 96-well Nucleofector^{TM} Kit (Lonza) and the 4D Nucleofector X Unit (Lonza) following manufacturer's instructions. Nucleofected cells were allowed to recover in mTeSR^{TM}-1 medium supplemented with Y-276932 (10 μM) and then underwent antibiotic selection with blasticidin (ThermoFisher Scientific; 10 μg/ml) following the previously published protocol (29, 30). Knockdown efficiency was evaluated by addition of doxycycline to the daily feeding media over the course of 5 days, collection of mRNA, and subsequent quantification of gene expression by qPCR.

Organoid Differentiation

Organoid differentiations were a modified protocol of previously a published spinal cord interneuron differentiation protocol (13). Human iPSCs were seeded at 125000 cells/cm2 in mTeSR^{TM}-1 medium supplemented with the small molecule Rho-associated coiled-coil kinase (ROCK) inhibitor Y-276932 (10 μM; Selleckchem) and small molecule GSK inhibitor CHIR99021 (2μM, 4μM, or 6μM; Selleckchem). Two days later, cells were singularized with Accutase (STEMCELL Technologies), counted using a Countess II FL (Life Technologies), and seeded into 800μm X 800μm PDMS microwell inserts in a 24 well plate (~270 wells/insert)(23). After ~18 hours, condensed organoids were transferred to rotary culture in 10cm dishes or 6-well plates in mTeSR^{TM}-1 medium supplemented with Y-276932 (10 μM; Selleckchem), CHIR99021 (2μM, 4μM, or 6μM; Selleckchem), ALK5 small molecule inhibitor SB431542 (10μM, Selleckchem), and small molecule BMP inhibitor LDN193189 (0.2μM, Selleckchem). Organoids were fed every other day for up to 17 days. Y-276932 was removed from the media at day 3. At day 5 organoids were transferred to Neural Induction Media (DMEM F:12 (Corning), N2 supplement (Life Technologies), L-Glutamine (VWR), 2μg/ml heparin (Sigma Aldrich), non-essential amino acids (Mediatech INC), penicillin-streptomycin (VWR), supplemented with fresh 0.4μg/ml ascorbic acid (Sigma Aldrich) and 10ng/ml brain derived neurotrophin factor (BDNF, R&D Systems)) supplemented with CHIR99021 (2μM, 4μM, or 6μM; Selleckchem), SB431542 (10μM, Selleckchem), and LDN193189 (0.2μM, Selleckchem). From day 7 onwards, organoids were fed with Neural Induction Media supplemented with retinoic acid (10nM, Sigma Aldrich), purmorphamine (300nM, EMD Millipore) and N-[N-(3,5-difluorophenacetyl)-L-alanyl]-S-phenylglycine t-butyl ester (DAPT D5942, 1μM, Sigma-Aldrich).

Organoid Elongation Imaging and Quantification

Day 5 organoids from a single 10cm dish were individually transferred using wide bore pipette tips into the center 60 wells of an uncoated ultra-low attachment 96-well plate (Corning), seeding exactly one organoid per well, with the remaining organoids maintained in rotary culture through day 7. Using an inverted Axio Observer Z1 (Zeiss) microscope with incubation (Zeiss Heating Unit XL S, maintained at 37 °C, 5% CO_2), all 60 wells were imaged using an AxioCam MRm (Zeiss) digital CMOS camera at 5x magnification (NA 0.16, 2.6 μm x 2.6

μm per pixel). Each well was imaged in TL Brightfield every 20 minutes for 48 hours giving a total of 145 frames. At the end of imaging (day 7), 31 organoids from the parallel rotary culture were imaged at 5x to generate a comparison image set.

To segment the organoids, all well images were first aligned by fitting a truncated quadratic curve to the average image intensity, then solving for the peak of maximum intensity, which was assumed to be the well center. Next, the average lighting inhomogeneity was calculated as the pixel-wise median of all 60 aligned well images, which was then subtracted from the individual aligned frames. After background correction, individual organoids were isolated by finding objects brighter than 0.83% of maximum intensity, but less than 3.0% of maximum intensity, with object size greater than 2,000 pixels, eccentricity greater than 0.1, and solidity greater than 40%. A bounding box 2 mm x 2 mm around the center of each of these objects was calculated and all frames of the time series cropped to this bounding box to reduce memory usage. To detect the region of maximum motion in the time series, the difference image between each pair of sequential images was calculated, and then the pixelwise standard deviation was calculated over all difference images in a given region. This standard deviation image was then thresholded at between 0.01 and 0.03 (AU) depending on the remaining lighting inhomogeneity in the image, producing a ring-shaped mask around the periphery of each organoid. Finally, using the interior of the mask as the organoid seed and the exterior as the background seed for the first frame, organoids were segmented using anisotropic diffusion (41), evolving the foreground and background seeds using the contour calculated from the previous frame for subsequent segmentations. Segmentation, labeling, and metrology were all performed using the python package sckit-image (42).

Segmentations were manually inspected for accuracy, with 45 of 60 determined as having no or only minor flaws, with the remaining 15 excluded from automated analysis. Using the high-quality segmentations only, each organoid time series was then analyzed to examine geometry change over time. For each contour at each time point, we calculated contour area, contour perimeter, minimum, maximum and mean distance from contour center of mass to the perimeter. As additional non-dimensional measures of shape, we calculated the ratio of maximum to minimum radius and organoid circularity. Organoids were also manually classified as “extending”, “partially extending”, or “non-extending” by examining each video. Organoids assigned to “extending” exhibited at least one, and at most two large protuberances that extended at least 100μm from the main body. Partially extending organoids exhibited at least one, and often many protuberances, all of which failed to extend robustly past the 100 μm demarcation. Non-extending organoids were any organoids that failed to generate any extensions over the observation period.

Dissection of Polarized Organoids

Dissections were performed on a SteREO Discovery.V8 Manual Stereo Microscope (ZEISS) and images were taken with an EP50 Microscope Digital Camera (Olympus). Day 9 organoids were transferred into 12 mL of 37°C PBS in a 10 cm dish. 2 mL of warmed PBS were also added to 2 wells of a 6-well plate. Using two fine point forceps, polarized elongated aggregates were immobilized and pulled or pinched apart. Using a p200 pipet with a cut tip, the ‘head’ and ‘tail’ halves of the organoids were collected and transferred to separate wells of the 6-well plate. After ~25 organoids were dissected, the collected halves were transferred to Eppendorf tubes and suspended in RLT buffer (RNAeasy Mini Kit; QIAGEN) for RNA extraction. Remaining, whole undissected organoids were also collected and suspended in RLT buffer for comparison. Standard RNA extraction was performed following manufacturer specifications.

Real Time Quantitative Polymerase Chain Reaction

Total RNA was isolated from organoid samples using an RNAeasy Mini Kit (QIAGEN) according to manufacturer’s instructions. Subsequently, cDNA was generated using an iScript cDNA Synthesis kit (BIORAD) and the reaction was run on a SimpliAmp thermal cycler (Life Technologies). Quantitative PCR reaction using Fast SYBR Green Master Mix (ThermoFisher Scientific) and run on a StepOnePlus Real-Time PCR system (Applied Biosciences). Relative gene expression was determined by normalizing to the housekeeping gene 18S rRNA, using the comparative threshold (C_T) method. Gene expression was displayed as fold change of each sample versus control. The primer sequences were obtained from the Harvard Primer bank or designed using the NCBI Primer-BLAST website (Table S1).

Due to low RNA abundance in the 'head' and 'tail' dissected organoids, PreAmp Master Mix (FLUIDIGM) was used to amplify cDNA. Briefly, 20 ng of cDNA were amplified per 5 µL reaction volume for 15 cycles on a SimpliAmp thermal cycler (Life Technologies). Amplified cDNA was diluted 5-fold using nuclease free water. 1 µL of amplified diluted cDNA was used for each 20 µL quantitative PCR reaction using Fast SYBR Green Master Mix (ThermoFisher Scientific) and run on a StepOnePlus Real-Time PCR system (Applied Biosciences), following normal qPCR methods described above.

Histology, Immunocytochemistry and Imaging

Organoids were fixed with 4% paraformaldehyde (VWR) for 40 minutes, washed three times with PBS. Organoids to be used for histology were embedded in HistoGel Specimen Processing Gel (Thermo Fisher) prior to paraffin processing. Parafin embedded samples were sectioned in 5µm sections, and subsequently stained for H&E. For immunofluorescent staining, slides were deparaffinized as for H&E staining. Epitope retrieval was performed by submersing slides in Citrate Buffer pH 6.0 (Vector Laboratories) in a 95 ºC water bath for 35 minutes. Samples were permeabilized in 0.2% Triton X-100 (Sigma-Aldrich) for 5min, blocked in 1.5% normal donkey serum (Jackson Immunoresearch) for 1 hour, and probed with primary antibodies against SOX2, PAX6, TBXT, NES, TUBB3, and CDH2 (Table S3) overnight at 4°C and secondary antibodies for 1 hour at RT. Nuclei were stained with a 1:10000 dilution of Hoechst 33342 (Thermo Fisher) included with secondary antibodies. Coverslips were mounted with anti-fade mounting medium (ProlongGold, Life Technologies) and samples were imaged on a Zeiss Axio Observer Z1 inverted microscope equipped with a Hamamatsu ORCA-Flash 4.0 camera.

Whole Mount Lightsheet Imaging

4% paraformaldehyde-fixed paraffin-embedded samples (see "*Histology, Immunocytochemistry, and Imaging*") were permeabilized with 1.5% Triton X-100 (Sigma-Aldrich) for 1 hour, blocked in 5% normal donkey serum (Jackson Immunoresearch) for 1 hour, and probed with primary and secondary antibodies (TableS3) overnight. Nuclei were stained with a 1:10000 dilution of Hoechst 33342 (Thermo Fisher) included with secondary antibodies. Samples were then embedded in 1.5% low melt agarose (BioReagent) and drawn up into ~1mm imaging capillaries and subsequently imaged on the Zeiss Z.1 Light sheet Microscope equipped with two PCO.edge SCMOS cameras at 5X and 20x (NA 1.34, aqueous objective).

Single Cell RNA Sequencing Sample and Library Preparation

Multiple organoid samples were combined and processed together using the MULTI-Seq technology (43). Organoids were singularized using Accutase (STEMCELL Technologies) and washed with cold PBS. Cells were resuspended in PBS with lipid-modified Anchor and Barcode oligonucleotides (gift from Zev Gartner, UCSF) and incubated on ice for 5 minutes. A co-Anchor oligo was then added in order to stabilize membrane retention of the barcodes incubated for an additional 5 minutes on ice. Excess lipid-modified oligos were quenched with 1% BSA in PBS, washed with cold 1% BSA solution, and counted using a Countess II FL (Life Technologies). Single cell GEMs and subsequent libraries were then prepared using the 10X Genomics Single Cell V2 protocol with an additional anchor specific primer during cDNA amplification to enrich barcode sequences (43). Short barcode sequences (approx. 65-100bp determined by Bioanalyzer) were purified from cDNA libraries with two sequential SPRI bead cleanups. Barcode library preparation was performed according to the KAPA HiFi Hotstart (Kapa Biosystems) protocol to functionalize with the P5 sequencing adapter and library-specific RPIX barcode. Purified ~173bp barcode fragments were isolated with another SPRI bead cleanup and validation by Bioanalyzer.

The sample library was sequenced on an Illumina NovaSeq yielding an average of 41,112 reads per cell and 6,444 cells. The MULTI-Seq barcode library was sequenced on an Illumina NextSeq yielding an average of 9,882 reads per barcode and enabling sample assignment for 4,681 of 6,124 unique UMIs detected (76.4% recovery), using the demultiplexing code provided by the MULTI-Seq protocol (43).

Genome Annotation, RNA-seq Read Mapping, and Estimation of Gene and Isoform Expression

The sample library was aligned to the human GRCh38 reference genome using Cell Ranger v1.2.0 (10x Genomics). Gene expression levels were assessed using the Seurat v3.0.0 analysis pipeline (44). First cells

were removed with fewer than 200 detected genes, fewer than 1,000 total detected transcripts, or which had greater than 10% mitochondrial gene expression. Next, expression levels were log normalized, and the top 2,000 variable genes calculated using the VST algorithm. The top 20 principal components were used to group cells into 6 clusters using a resolution of 0.2. Finally, top markers were detected for each cluster by detecting the top differentially expressed genes between one cluster and the remaining data set, where at least 25% of cells in the cluster expressed the gene and the gene was expressed at least 0.25 $\log_2$ fold-change different from the remaining population. Clusters and gene expression were visualized on a two-dimensional UMAP projection of the first 20 principal components.

Cluster Analysis
To assign cluster identity, the top markers for each cluster were tested for GO term enrichment using the biological process "enrichGO" function in the R package "clusterProfiler" v3.12 (45). In addition, differentiation maturity in each cluster was assessed by examining expression level of panels of early neuroectoderm markers, proliferation markers, markers of neuron fate commitment, and markers of cell types present in neural tube formation and axial extension (22, 46). Finally, to assess anterior-posterior position of each, panels of HOX genes, as well as marker genes of Wnt and FGF signaling were examined to assign rough position of each cluster along the head-tail axis (7, 9, 47).

RNAScope
In situ hybridization for HOXB1, HOXC6, HOXB9 (probe information in Table S4) was performed on sections of 4% paraformaldehyde-fixed paraffin-embedded samples (see "*Histology, Immunocytochemistry, and Imaging*") using the RNAscope Multiplex Fluorescent Reagent Kit v2 (Advanced Cell Diagnostics) and following the protocol outlined in User Manual 323100-USM. Sections were imaged on a Zeiss Axio Observer Z1 inverted microscope equipped with a Hamamatsu ORCA-Flash 4.0 camera.

Statistical Analysis
Each experiment was performed with at least three biological replicates. Multiple comparisons were used to compare multiple groups followed by unpaired T-tests between two groups subject to a post-hoc Bonferroni correction. In gene expression analysis, three replicates were used for each condition, and all gene expression was normalized to control wildtype populations. Significance was specified as P-values< 0.05 unless otherwise specified in figure legends. All error bars represent 95% confidence bounds of the data.

Data Availability
The single cell RNA-seq data generated from this study will be made available on the Gene Expression Omnibus upon acceptance. The data analysis code generated in the live imaging analysis studies will be made available via GitHub repository upon acceptance.

Supplementary Materials

Fig. S1: Time lapse imaging of organoid elongation.
Fig. S2: Organoid culture density within 6-well plates.
Fig. S3: Organoid culture volume and density changes emergence of extensions.
Fig. S4: Internal structure differences between non-extending and extending organoids.
Fig. S5: TBXT streak within extending organoids.
Fig. S6: TBXT patterns before extension morphology.
Fig. S7: Neural markers over time in extending organoids.
Fig. S8: Apical-basal polarity in extending organoids over time.
Fig. S9: Bilayer of cells in extending organoids.
Fig. S10: Dissections of extending organoids to isolate anterior and posterior regions.
Fig. S11: Changes to morphological extensions with increasing Wnt signaling.
Fig. S12: Gene expression within extending and non-extending organoids.

Movie S1: Elongating organoid dynamics.

Movie S2: Non-elongating organoid dynamics.
Movie S3: TBXT and SOX2 localization in a non-elongating organoid.
Movie S4: TBXT and SOX2 localization in an elongating organoid.
Movie S5: COL IV and ZO1 localization in a non-elongating organoid.
Movie S6: COL IV and ZO1 localization in an elongating organoid.
Movie S7: β III tubulin and Nestin localization in a non-elongating organoid.
Movie S8: β III tubulin and Nestin localization in an elongating organoid.

Table S1: qPCR Primers.
Table S2: CRISPRi guides.
Table S3: Antibodies.
Table S4: RNAscope Probes.

References:

1. Steventon B, Duarte F, Lagadec R, Mazan S, Nicolas JF, Hirsinger E. Species-specific contribution of volumetric growth and tissue convergence to posterior body elongation in vertebrates. Development. 2016;143(10):1732-41.
2. Wilson V, Olivera-Martinez I, Storey KG. Stem cells, signals and vertebrate body axis extension. Development. 2009;136(10):1591-604.
3. Schiffmann Y. Symmetry breaking and convergent extension in early chordate development. Progress in Biophysics and Molecular Biology. p. 209-31.
4. Cambray N, Wilson V. Two distinct sources for a population of maturing axial progenitors. 2007.
5. Wymeersch FJ, Huang Y, Blin G, Cambray N, Wilkie R, Wong FC, et al. Position-dependent plasticity of distinct progenitor types in the primitive streak. 2016.
6. Beddington RS, Robertson EJ. Axis development and early asymmetry in mammals. Cell. 1999;96(2):195-209.
7. Bel-Vialar S, Itasaki N, Krumlauf R. Initiating Hox gene expression: in the early chick neural tube differential sensitivity to FGF and RA signaling subdivides the HoxB genes in two distinct groups. Development. 2002;129(22):5103-15.
8. Diez del Corral R. Opposing FGF and Retinoid Pathways Control Ventral Neural Pattern, Neuronal Differentiation, and Segmentation during Body Axis Extension. Neuron.40(1):65-79.
9. Carpenter EM. Hox Genes and Spinal Cord Development. Developmental Neuroscience. 2020;24(1):24-34.
10. Liem KF, Tremml G, Roelink H, Jessell TM. Dorsal Differentiation of Neural Plate Cells Induced by BMP-Mediated Signals from Epidermal Ectoderm. Cell. 1995;82:969-79.
11. Ericson J. Graded Sonic Hedgehog Signaling and the Specification of Cell Fate in the Ventral Neural Tube. Cold Spring Harbor Symposia on Quantitative Biology. 1997;62:451-66.
12. McMahon JA, Takada S, Zimmerman LB, Fan CM, Harland RM, McMahon AP. Noggin-mediated antagonism of BMP signaling is required for growth and patterning of the neural tube and somite. Genes Dev. 1998;12(10):1438-52.
13. Butts JC, McCreedy DA, Martinez-Vargas JA, Mendoza-Camacho FN, Hookway TA, Gifford CA, et al. Differentiation of V2a interneurons from human pluripotent stem cells. Proc Natl Acad Sci U S A. 2017;114(19):4969-74.
14. Gouti M, Tsakiridis A, Wymeersch FJ, Huang Y, Kleinjung J, Wilson V, et al. In vitro generation of neuromesodermal progenitors reveals distinct roles for wnt signalling in the specification of spinal cord and paraxial mesoderm identity. PLoS Biol. 2014;12(8):e1001937.
15. Lancaster MA, Knoblich JA. Organogenesis in a dish: Modeling development and disease using organoid technologies. 2014.
16. Faustino Martins J-M. Self-Organizing 3D Human Trunk Neuromuscular Organoids. Cell Stem Cell. 2020;26(2):172-86.e6.
17. Turner DA, Hayward PC, Baillie-Johnson P, Rué P, Broome R, Faunes F, et al. Wnt/β-catenin and FGF signalling direct the specification and maintenance of a neuromesodermal axial progenitor in ensembles of mouse embryonic stem cells. 2014.

18. Beccari L, Moris N, Girgin M, Turner DA, Baillie-Johnson P, Cossy A-C, et al. Multi-axial self-organization properties of mouse embryonic stem cells into gastruloids. Nature. 2018;562(7726):272-6.
19. Lippmann ES, Williams CE, Ruhl DA, Estevez-Silva MC, Chapman ER, Coon JJ, et al. Deterministic HOX Patterning in Human Pluripotent Stem Cell-Derived Neuroectoderm. Stem Cell Reports. 2015;4(4):632-44.
20. Mallo M, Wellik DM, Deschamps J. Hox Genes and Regional Patterning of the Vertebrate Body Plan. Dev Biol. 2010;344(1):7-15.
21. Yamaguchi TP. Heads or tails: Wnts and anterior–posterior patterning. Current Biology. 2001;11(17).
22. Henrique D, Abranches E, Verrier L, Storey KG. Neuromesodermal progenitors and the making of the spinal cord. Development. 2015;142(17):2864-75.
23. Hookway TA, Butts JC, Lee E, Tang H, McDevitt TC. Aggregate formation and suspension culture of human pluripotent stem cells and differentiated progeny. Methods. 2016;101:11-20.
24. Carpenedo RL, Sargent CY, McDevitt TC. Rotary suspension culture enhances the efficiency, yield, and homogeneity of embryoid body differentiation. Stem Cells. 2007;25(9):2224-34.
25. Osafune K, Caron L, Borowiak M, Martinez RJ, Fitz-Gerald CS, Sato Y, et al. Marked differences in differentiation propensity among human embryonic stem cell lines. Nature Biotechnology. 2008;26(3):313-5.
26. Nazareth EJ, Ostblom JE, Lücker PB, Shukla S, Alvarez MM, Oh SK, et al. High-throughput fingerprinting of human pluripotent stem cell factor responsiveness and lineage induction bias. Nat Methods. 2013;10(12):1225-31.
27. McMahon JA, Takada S, Zimmerman LB, Fan C-M, Harland RM, McMahon AP. Noggin-mediated antagonism of BMP signaling is required for growth and patterning of the neural tube and somite. Genes & Development. 1998;12:1438-52.
28. Bachiller D, Klingensmith J, Shneyder N, Tran U, Anderson R, Rossant J, et al. The role of chordin/Bmp signals in mammalian pharyngeal development and DiGeorge syndrome. 2003.
29. Libby AR, Joy DA, So PL, Mandegar MA, Muncie JM, Mendoza-Camacho FN, et al. Spatiotemporal mosaic self-patterning of pluripotent stem cells using CRISPR interference. Elife. 2018;7.
30. Mandegar MA, Huebsch N, Frolov EB, Shin E, Truong A, Olvera MP, et al. CRISPR Interference Efficiently Induces Specific and Reversible Gene Silencing in Human iPSCs. Cell Stem Cell. 2016;18(4):541-53.
31. Lancaster MA, Renner M, Martin C-A, Wenzel D, Bicknell LS, Hurles ME, et al. Cerebral organoids model human brain development and microcephaly. Nature. 2013;501(7467):373-9.
32. Renner M, Lancaster MA, Bian S, Choi H, Ku T, Peer A, et al. Self-organized developmental patterning and differentiation in cerebral organoids | The EMBO Journal. The EMBO Journal. 2020.
33. Sato T, Vries RG, Snippert HJ, Wetering Mvd, Barker N, Stange DE, et al. Single Lgr5 stem cells build crypt-villus structures in vitro without a mesenchymal niche. Nature. 2009;459(7244):262-5.
34. Eiraku M, Takata N, Ishibashi H, Kawada M, Sakakura E, Okuda S, et al. Self-organizing optic-cup morphogenesis in three-dimensional culture. Nature. 2011;472(7341):51-6.
35. Harrison SE, Sozen B, Christodoulou N, Kyprianou C, Zernicka-Goetz M. Assembly of embryonic and extraembryonic stem cells to mimic embryogenesis in vitro. 2017.
36. Brink SCvd, Alemany A, Batenburg Vv, Moris N, Blotenburg M, Vivié J, et al. Single-cell and spatial transcriptomics reveal somitogenesis in gastruloids. Nature. 2020:1-5.
37. Bhaduri A, Andrews MG, Leon WM, Jung D, Shin D, Allen D, et al. Cell stress in cortical organoids impairs molecular subtype specification. Nature. 2020;578(7793):142-8.
38. Miyaoka Y, Chan AH, Judge LM, Yoo J, Huang M, Nguyen TD, et al. Isolation of single-base genome-edited human iPS cells without antibiotic selection. Nature Methods. 2014;11(3):291-3.
39. Ludwig TE, Bergendahl V, Levenstein ME, Yu J, Probasco MD, Thomson JA. Feeder-independent culture of human embryonic stem cells. Nat Methods. 2006;3(8):637-46.
40. Park S, Kim D, Jung YG, Roh S. Thiazovivin, a Rho kinase inhibitor, improves stemness maintenance of embryo-derived stem-like cells under chemically defined culture conditions in cattle. Anim Reprod Sci. 2015;161:47-57.
41. Random Walks for Image Segmentation - IEEE Journals & Magazine: IEEE; of Publication: 25 September 2006.

42. Walt Svd, Stellenbosch University S, South Africa, stefan@sun.ac.za, Schönberger JL, Department of Computer Science UoNCaCH, Chapel Hill, NC, USA, Nunez-Iglesias J, et al. scikit-image: image processing in Python. PeerJ. 2014;2.
43. McGinnis CS, Patterson DM, Winkler J, Conrad DN, Hein MY, Srivastava V, et al. MULTI-seq: sample multiplexing for single-cell RNA sequencing using lipid-tagged indices. Nature Methods. 2019;16(7):619-26.
44. Butler A, Hoffman P, Smibert P, Papalexi E, Satija R. Integrating single-cell transcriptomic data across different conditions, technologies, and species. Nature Biotechnology. 2018;36(5):411-20.
45. Yu G, Wang LG, Han Y, He QY. clusterProfiler: an R package for comparing biological themes among gene clusters. Omics. 2012;16(5):284-7.
46. Tanabe Y, Jessell TM. Diversity and Pattern in the Developing Spinal Cord. 1996.
47. Diez del Corral R, Storey KG. Opposing FGF and retinoid pathways: a signalling switch that controls differentiation and patterning onset in the extending vertebrate body axis. Bioessays. 2004;26(8):857-69.

Acknowledgements:
We would like to thank the Gladstone Light Microscopy and Histology Core, the Gladstone Stem Cell Core, and the Gladstone Graphics Team for their support and experimental expertise.

Author contributions:
ARGL, DAJ, and TCM were responsible for the conceptualization of the project and designing experiments. Differentiations were conducted by ARGL, DAJ, NHE, EAB, and EAG. Single cell RNA sequencing preparation and analysis were performed by ARGL, DAJ, NHE, and MZK. Image analysis script was written and implemented by DAJ and ARGL. Histological sectioning and staining were conducted by DAJ, NHE, EAB, and EAG. Light sheet microscopy and analysis was conducted by ARGL, DAJ, and EAG. Quantitative PCR was done by ARGL, DAJ, NHE, EAB, and MZK. RNAscope sample preparation and analysis was performed by ARGL. Cell lines were generated by ARGL, DAJ, MZK, and NMC. ARGL and DAJ wrote the original manuscript with input from all co-authors. ARGL prepared the figures with input from all co-authors.

Competing Interests:
Authors declare no competing interests.

Figures:
Figure 1

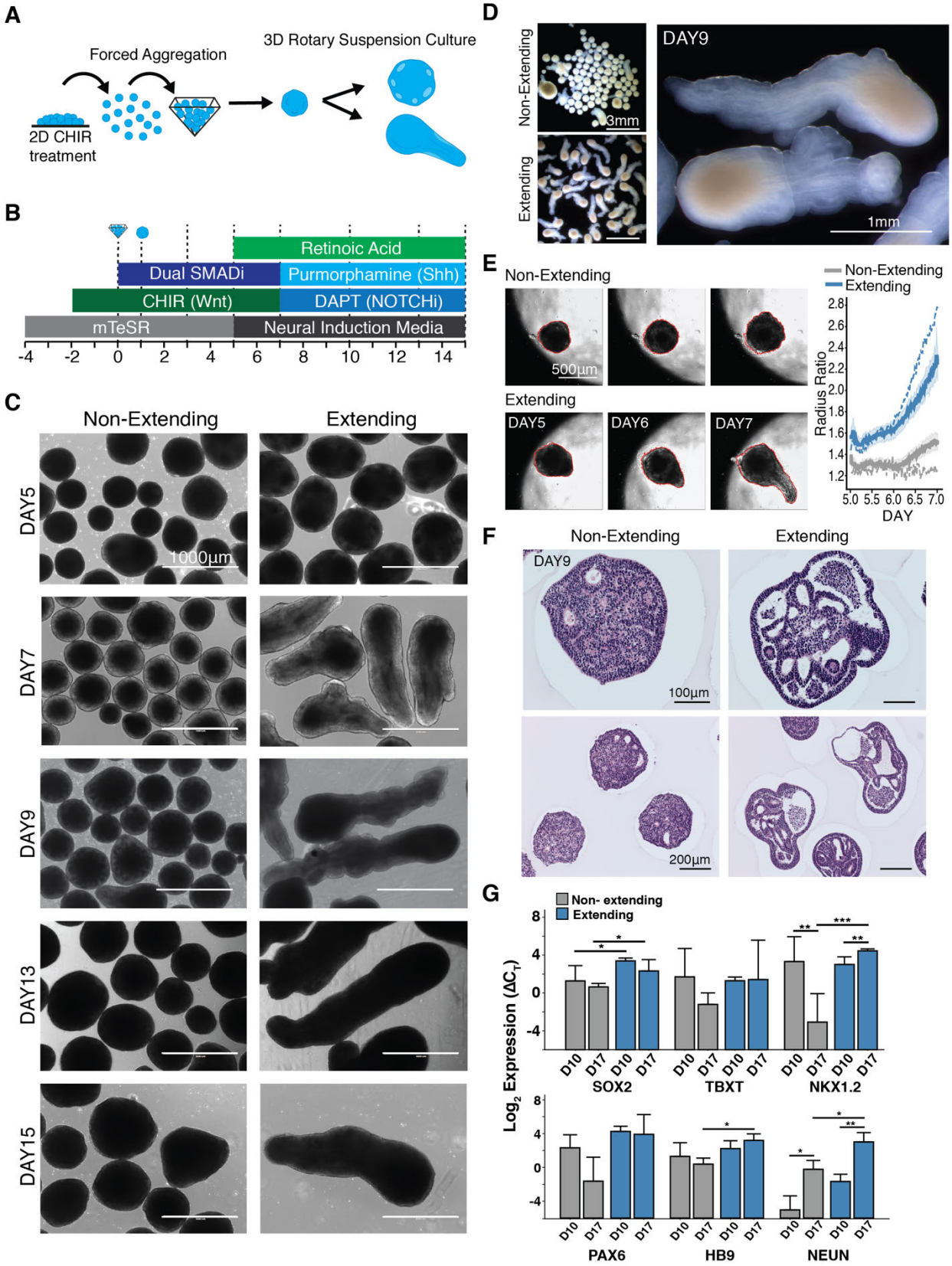

Figure 1: Emergence of axial extensions from neuronal organoids. A-B) Schematic of 3D culture experimental set up and differentiation protocol timeline. **C)** Brightfield images of extending and non-extending organoids from days 5 to 15 of differentiation. **D)** Stereoscope images of extending and non-extending organoids at day 9 of differentiation. **E)** (LEFT) Frames from video time-course tracking organoid extensions in static 96 well plate culture. (RIGHT) Quantification of radius ratios from day 5 to 7 of extending (blue) and non-extending (grey) organoids. Solid lines represent the mean ratio (dark color) with 95 percent confidence interval (light color; n= 24 non-elongating, n= 36 elongating). Dotted lines are the two pictured organoids on the left. **F)** Histology of sectioned non-extending and extending organoids at day 9 of differentiation. **G)** qPCR analysis of day 10 and 17 organoids where * indicates $p<0.05$, ** indicates $p<.01$, and *** indicates $p<.001$.

Figure 2

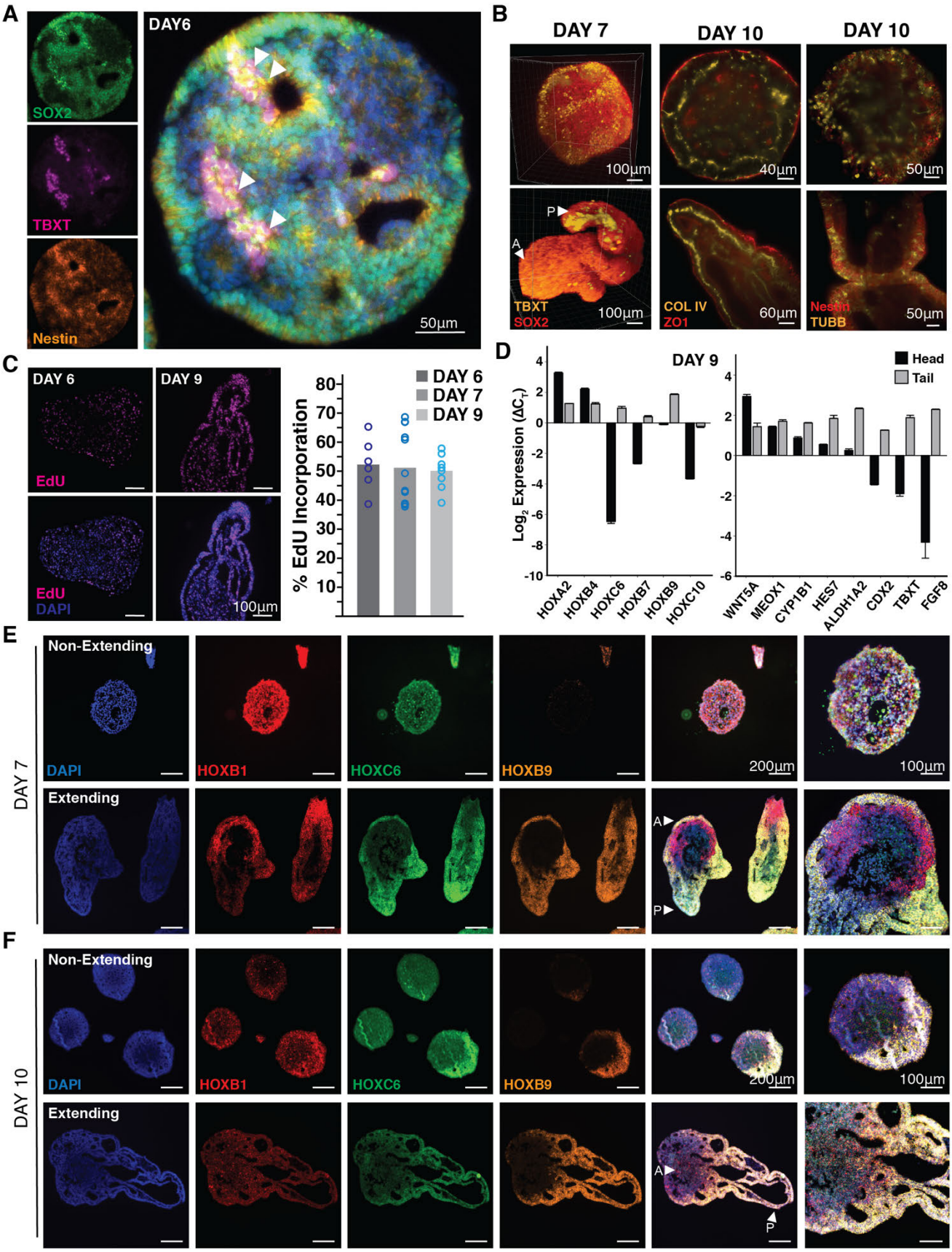

Figure 2: Morphology and organization of organoids. A) Immunofluorescence staining of an extending organoid at day 6 of differentiation. White arrows indicate SOX2(+)TBXT(+) cells. **B)** 3D renderings and optical sections from light-sheet microscopy of non-extending (top) and extending (bottom) organoids stained for TBXT, SOX2, COL IV, ZO1, Nestin, βIII-Tubulin (TUBB) (arrows mark anterior (A) and posterior (P) axis of organoids). **C)** (LEFT) Immunofluorescence images of EdU incorporation in extending organoids. (RIGHT) Quantification of EdU incorporation as percent of cells. **D)** qPCR data of HOX genes and region specific genes in anterior vs. posterior of organoids. **E-F)** RNAscope of sectioned organoids with probes for HOX genes marking different regions of the spine at day 7 and 10 of differentiation (arrows mark anterior (A) and posterior (P) axis of organoids).

Figure 3

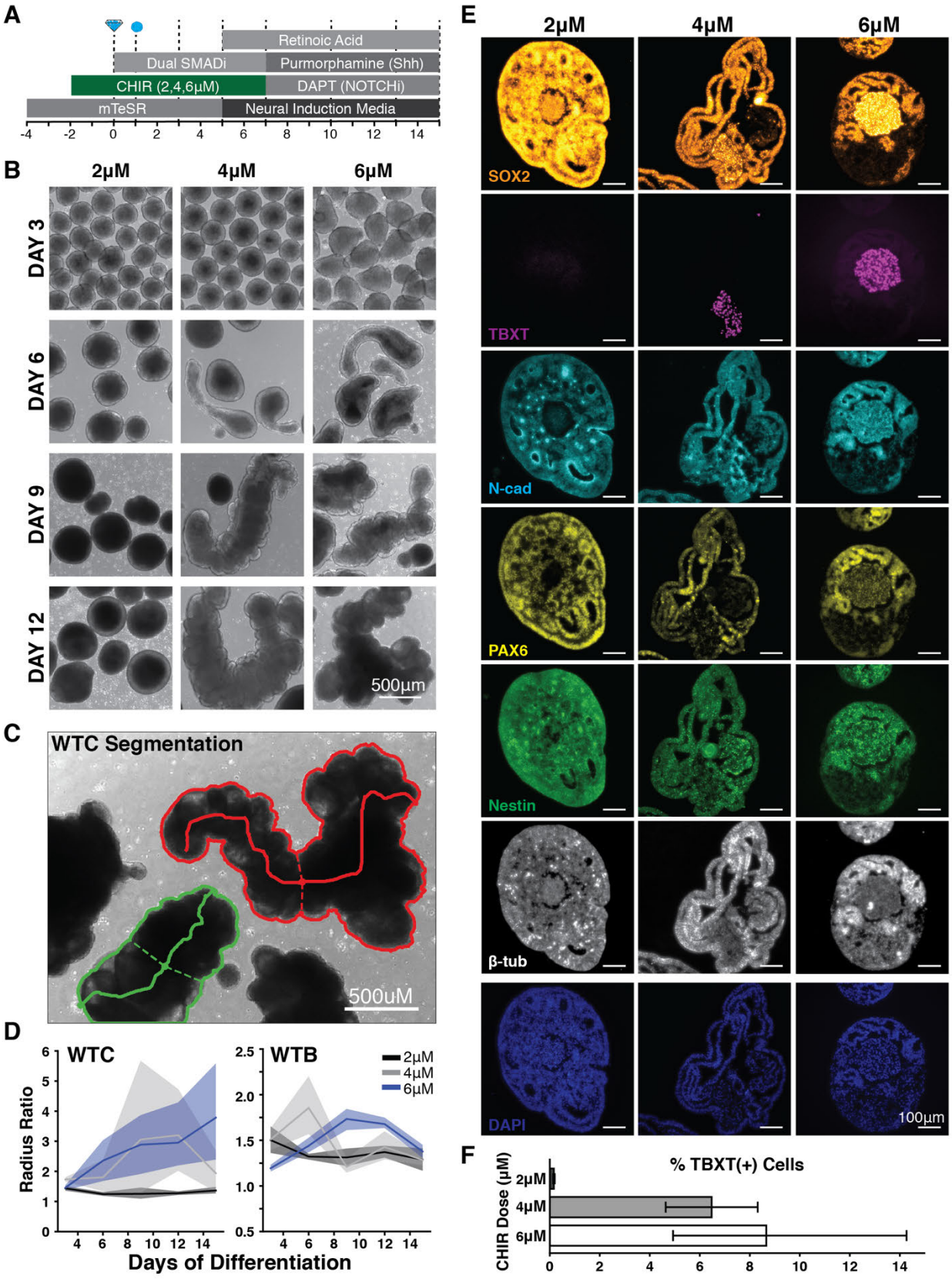

Figure 3: Wnt mediated increase in extensions and SOX2(+)TBXT(+) progenitor populations. A) Schematic of differentiation protocol timeline with increased CHIR dosing. **B)** Brightfield images of differentiation with increased CHIR doses conducted in the WTC hiPS cell line. **C)** Example image of organoid segmentation to quantify major and minor axis length. **D)** Quantification of cell lines WTC and WTB length of extension shown as radius ratio (ie. length to width) with increasing doses of CHIR. **E)** Immunofluorescence of paraffin sectioned organoids at day 10 of differentiation from 2μM, 4μM, and 6μM CHIR concentrations. **F)** Image quantification of TBXT(+) cells in stained light-sheet volumes of day 10 organoids differentiated with 2μM, 4μM, and 6μM CHIR.

Figure 4

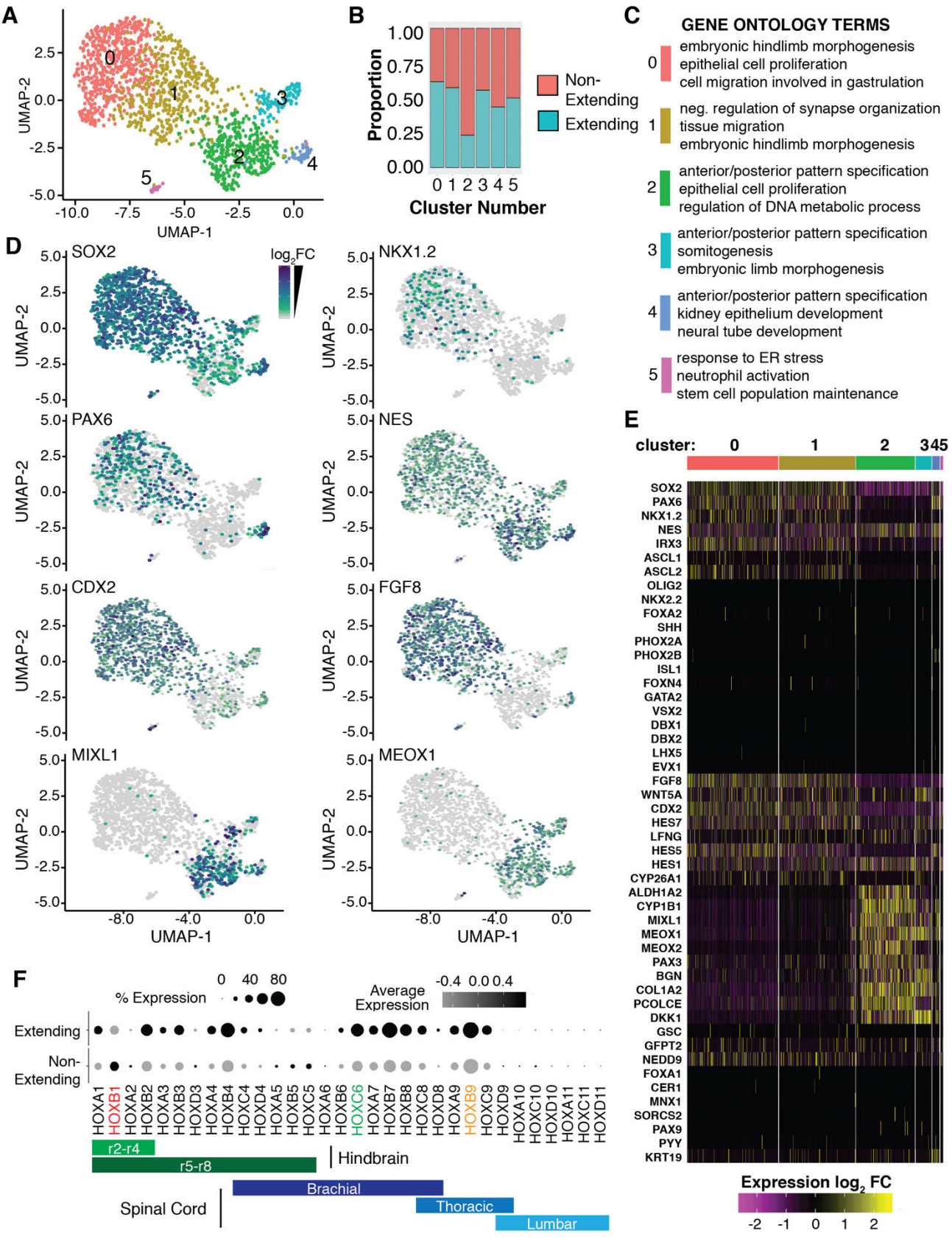

Figure 4: Gene expression in non-extending and extending organoids. A) UMAP of n=1566 cells from extending and non-extending organoids at day 10 of differentiation. **B)** Proportions of non-extending vs. extending organoids within each cluster. **C)** Gene Ontology terms assigned to identified clusters. **D)** UMAPs marking cells expressing SOX2, NKX1.2, PAX6, NES, CDX2, FGF8, MIXL1, and MEOX1. Color scale indicates a normalized increase in $\log_2$ fold change from min expression to max expression of the respective gene. **E)** Heat map showing normalized expression levels of genes associated with ventral interneuron specification, caudalizing factors, mesoderm and endoderm specification. **F)** Detected HOX gene expression across elongating and non-elongating organoids. Schematic depicting HOX gene regions of the spinal cord.

Figure 5

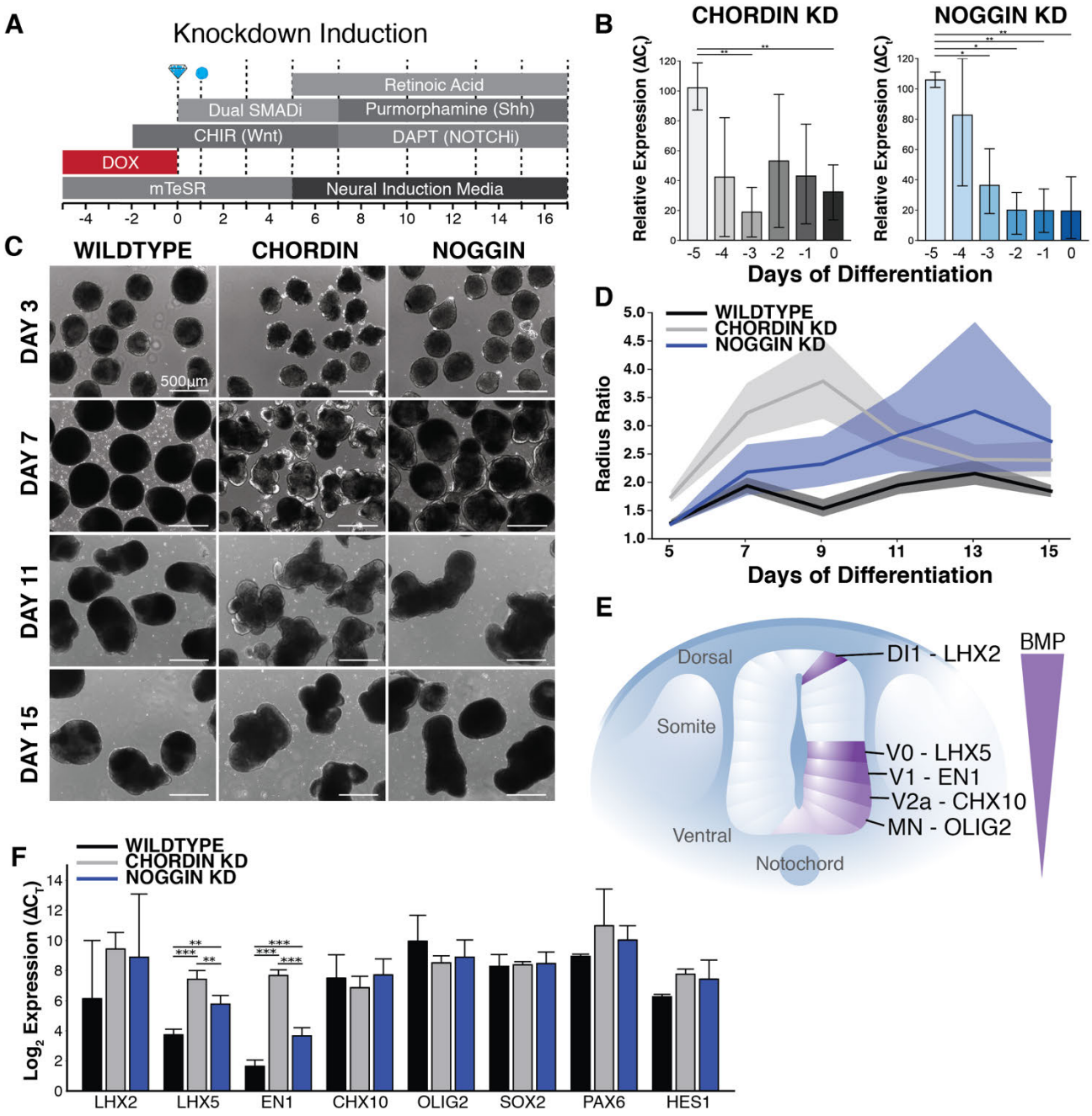

Figure 5: Manipulation of endogenous BMP signaling by CRISPR interference. A) Schematic of differentiation protocol timeline with knockdown induction. **B)** Quantification of Noggin and Chordin knockdown efficiency by reduction in mRNA expression levels measured by qPCR. **C)** Brightfield images of differentiation time course of knockdown hiPSC lines. **D)** Quantification of organoid length displayed as aspect ratio in response to knockdown. **E)** Schematic depicting BMP signaling and progenitor specification within the developing neural tube. **F)** Quantification of mRNA expression of progenitor specific transcription factors by qPCR at day 17 of differentiation (n=3). Error bars depict standard deviations. Significance depicted by * indicating $p<0.05$, ** indicating $p<.01$, and *** indicating $p<.001$.

Supplementary Figures:

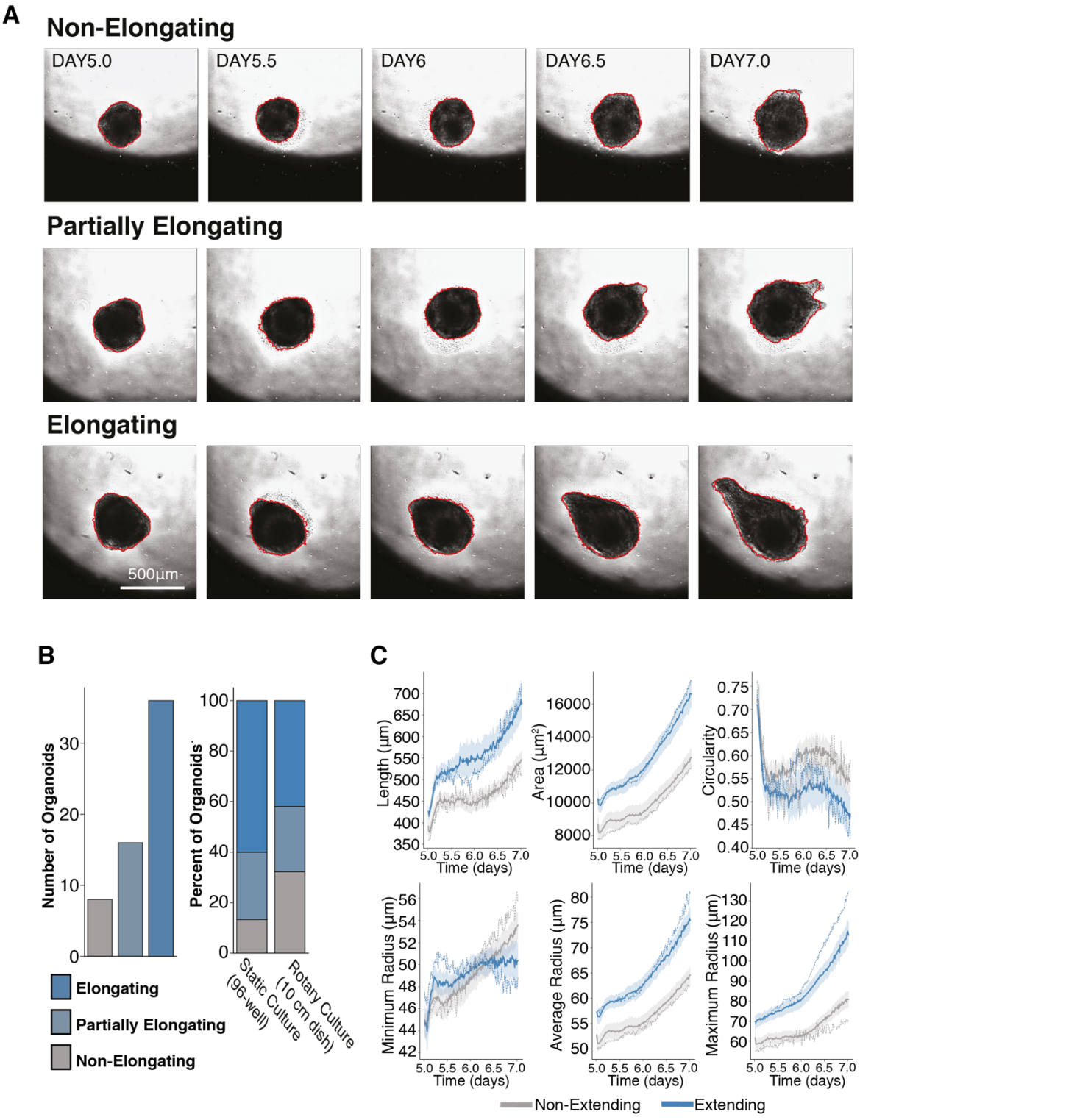

Figure S1: Time lapse imaging of organoid elongation. A) Frames from supplementary movies (**MS1, MS2**) depicting time-course of extension from days 5-7 of differentiation. **B)** Quantification of organoid extensions by number of extension and percent of the entire sample (n = 8 non-extending, n= 16 partial extending, n = 36 extending organoids). **C)** Quantification of length, area, circularity, and radius of extending and non-extending organoids. Dark solid line represents the mean value with 95 percent confidence interval depicted by the surrounding light color (n= 24 non-elongating, n= 36 elongating).

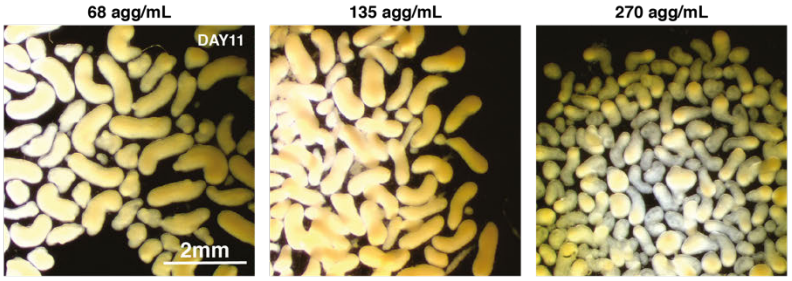

Figure S2: Organoid culture density within 6-well plates. Stereoscope images of extending organoids at day 11 of differentiation when cultured at different densities in rotary culture.

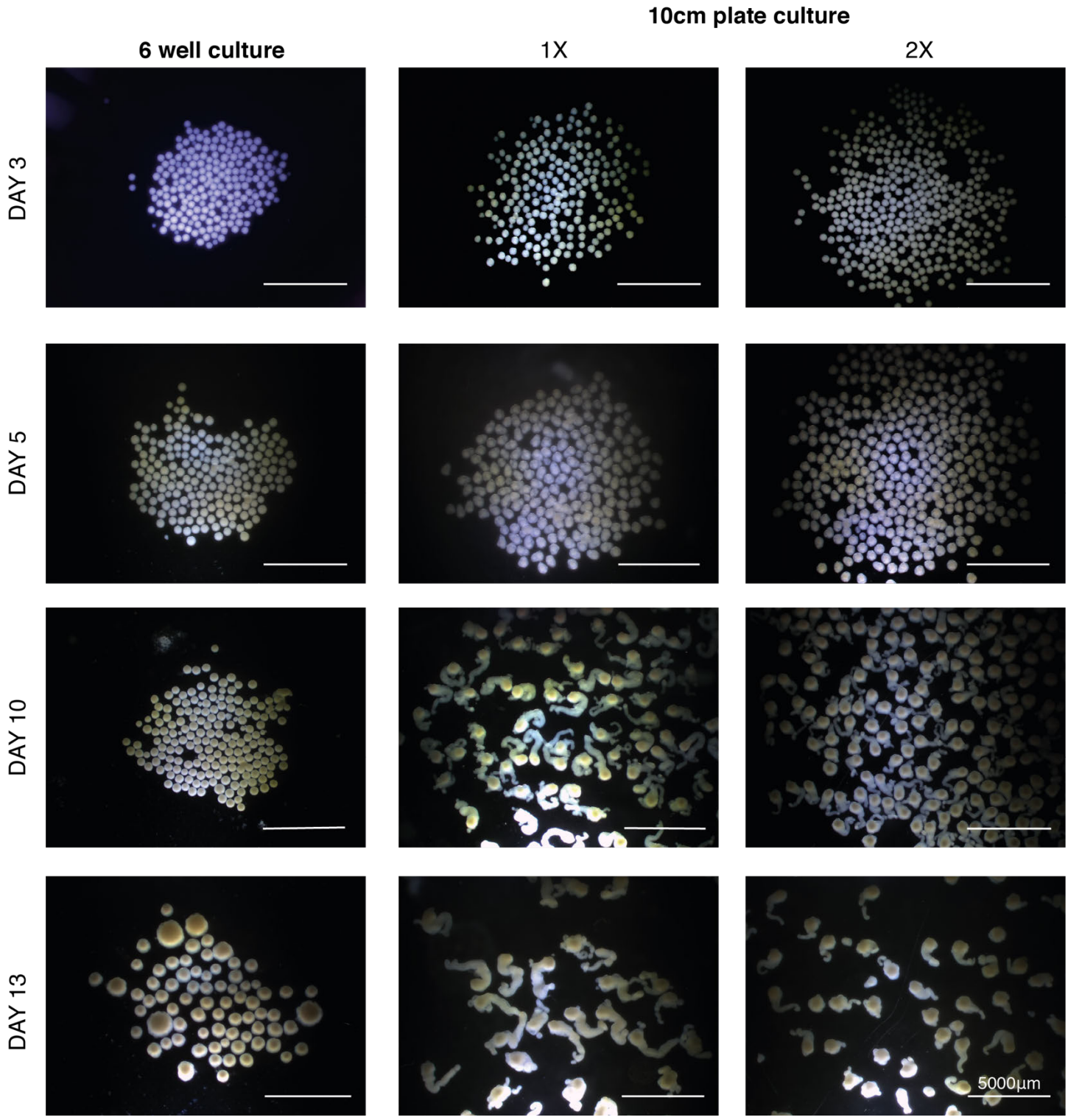

Figure S3: Organoid culture density changes morphology of extensions. Stereoscope images of organoids grown at different densities where 1X = 270 organoids. 6-well culture indicates 1X per well, 10cm dish culture indicates 1X or 2X per dish.

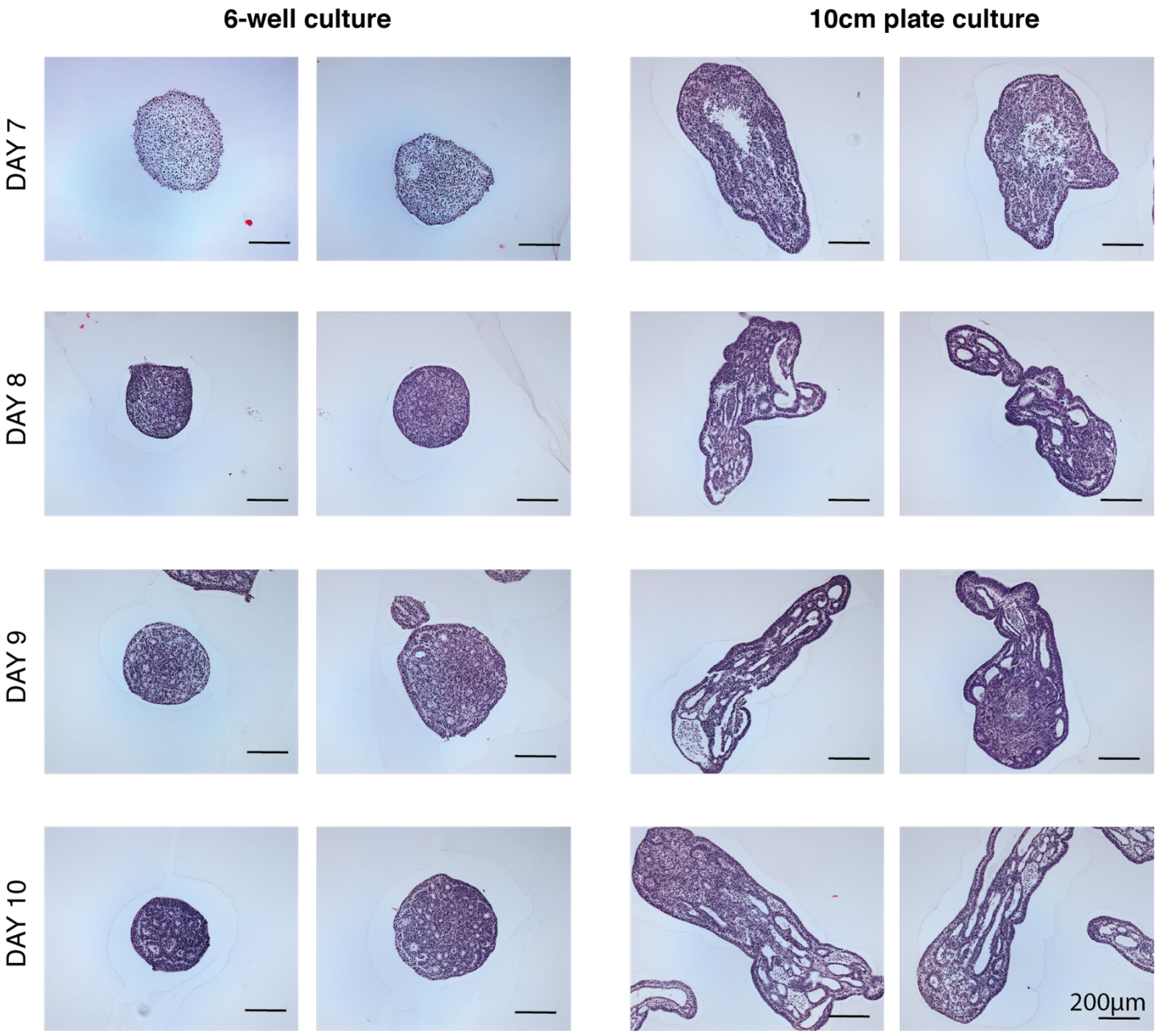

Figure S4: Internal structure differences between non-extending and extending organoids. Histological stains on paraffin sections of organoids from days 7 – 10 of differentiation.

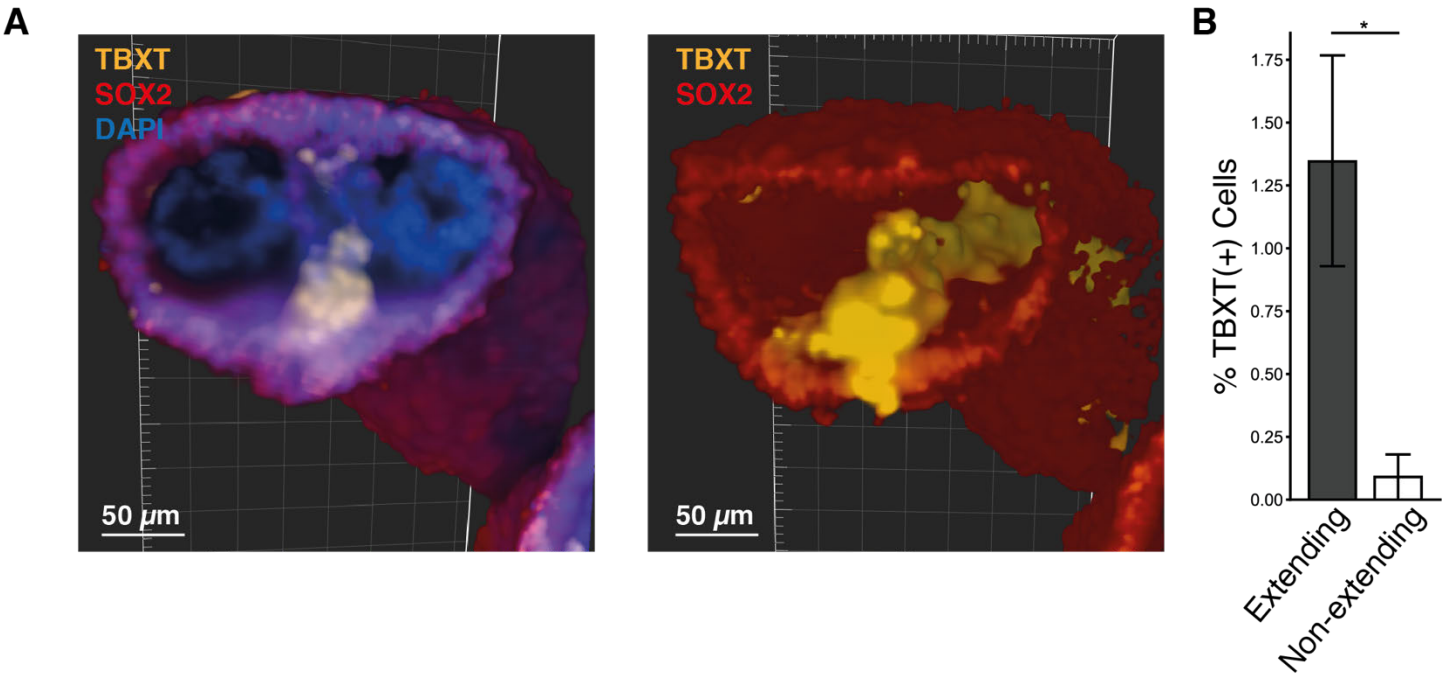

Figure S5: TBXT streak within extending organoids. A) 3D reconstruction of light-sheet microscopy taken of the posterior of extending organoids. **B)** Histogram of the percent brachyury (TBXT) positive cells in extending compared to non-extending organoids (* signifies $p<0.05$).

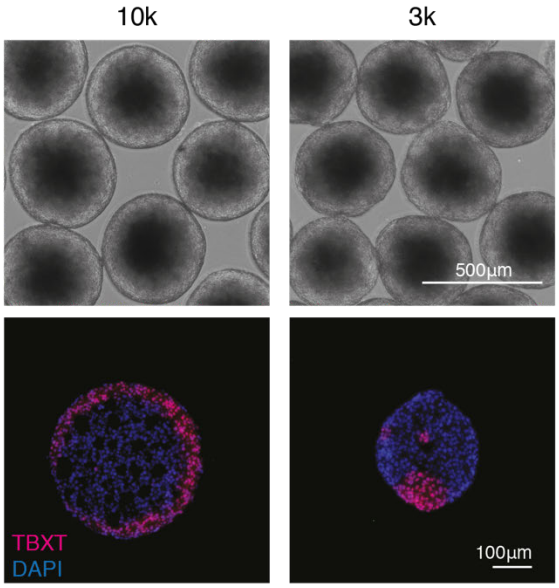

Figure S6: TBXT patterns before extension morphology. Paraffin sections of organoids before appearance of extensions at Day 3 of differentiation, labeled for TBXT, with matching brightfield images.

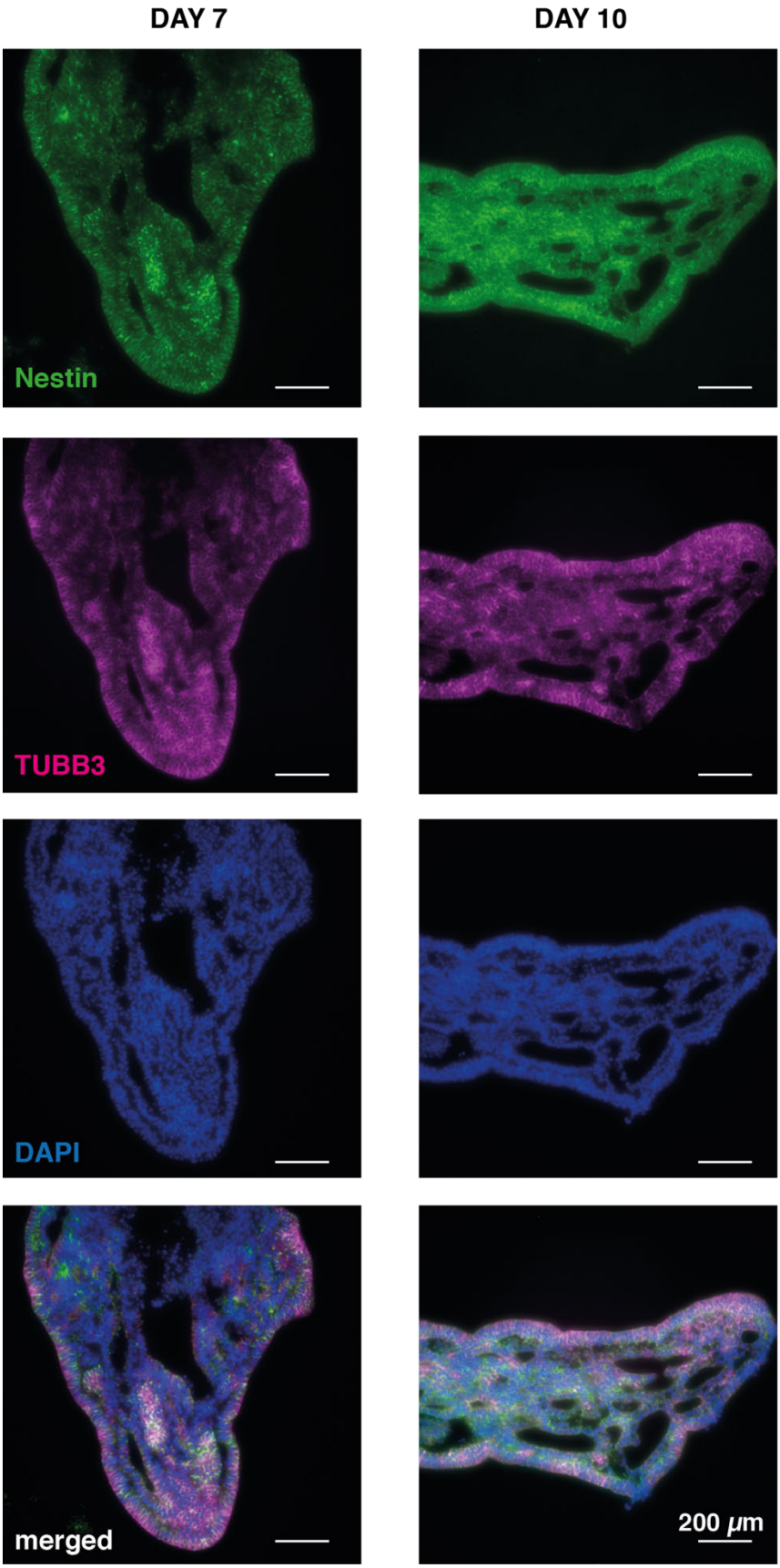

Figure S7: Neural markers over time in extending organoids. Immunofluorescence of paraffin sections of extending organoids at day 7 and day 10 of differentiation.

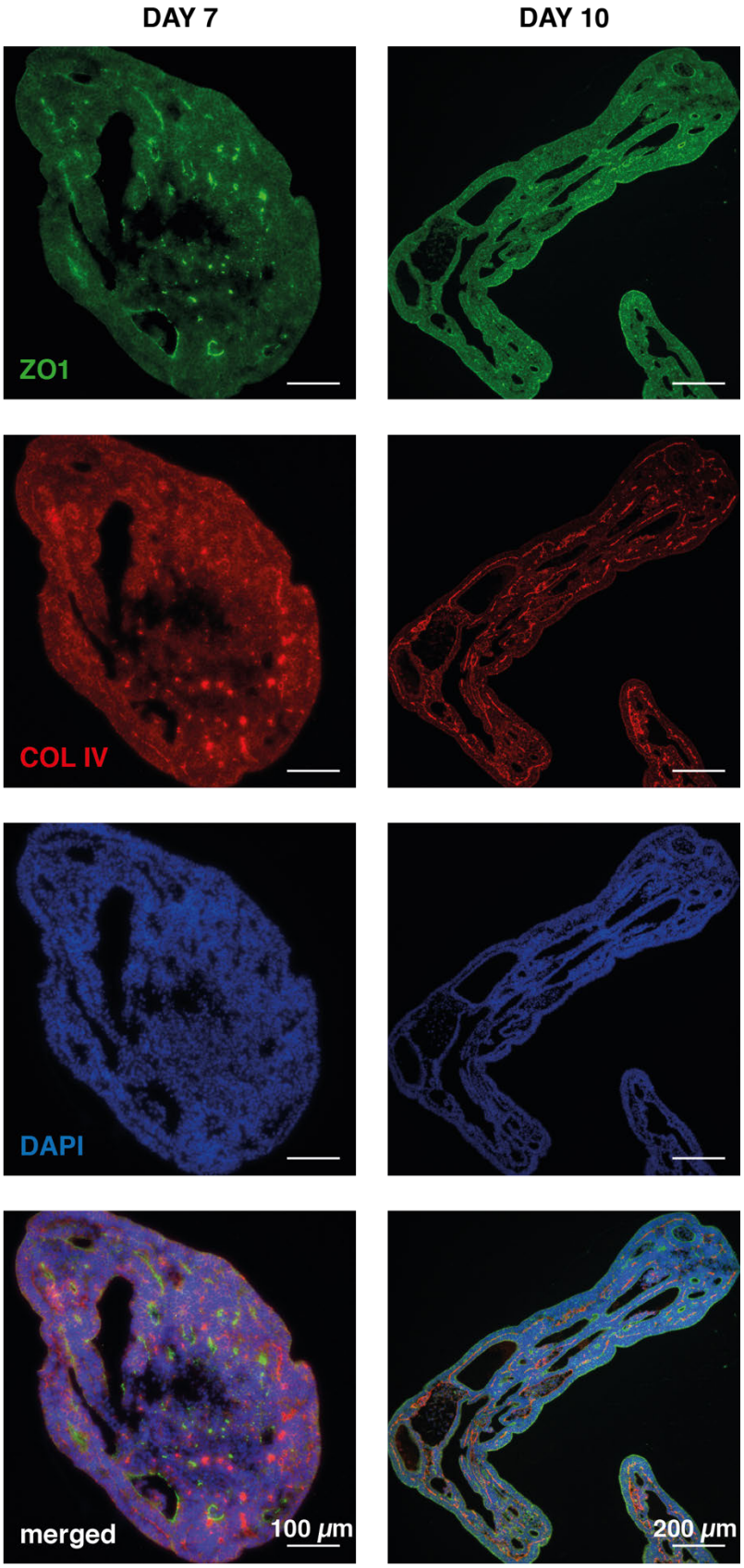

Figure S8: Apical-Basal polarity in extending organoids over time. Immunostaining of paraffin sections of extending organoids at day 7 and 10 of differentiation for markers of basement membrane (COL IV) and tight junctions (ZO1).

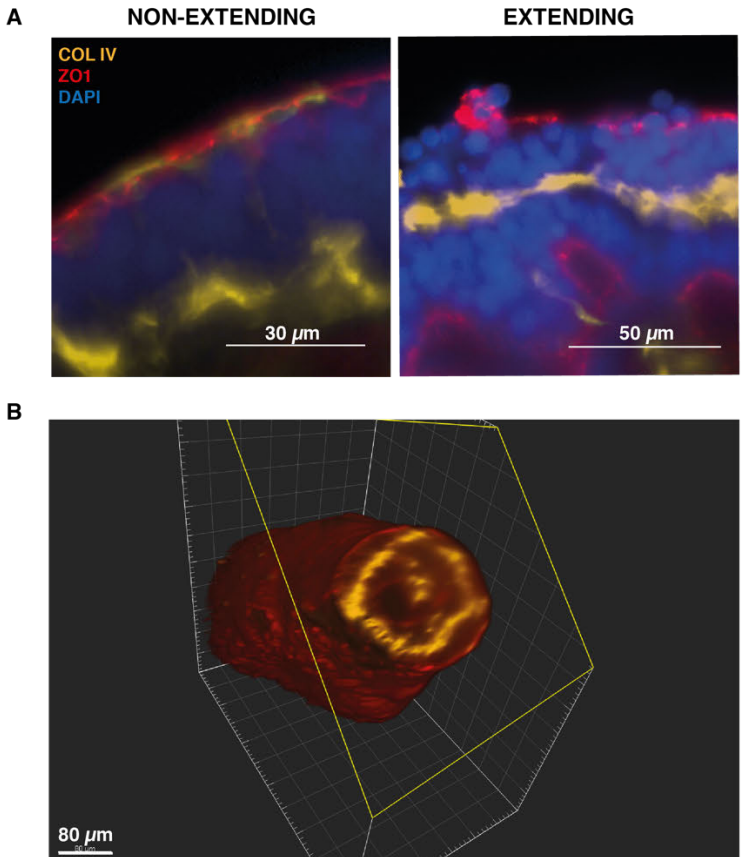

Figure S9: Bilayer of cells in extending organoids. A) optical sections from light-sheet imaging of extending and non-extending organoids stained for COL IV and ZO1. **B)** 3D reconstruction showing internal ring of basement membrane within the posterior extensions.

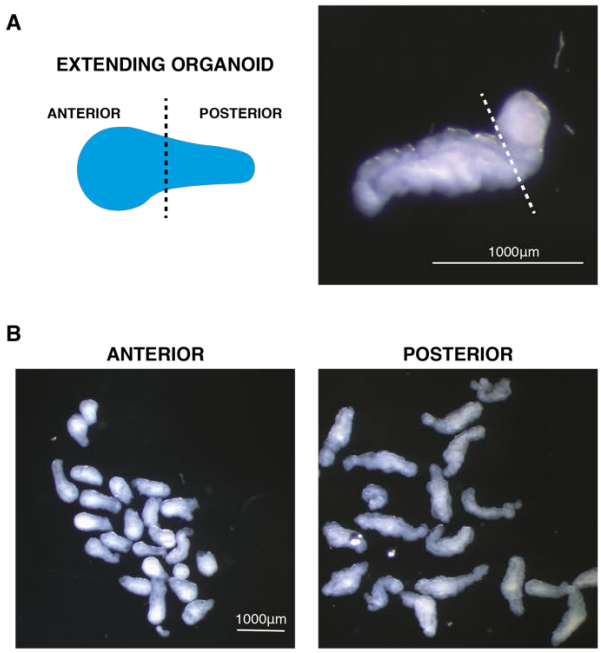

Figure S10: Dissections of extending organoids to isolate anterior and posterior regions. A) Schematic and example of anterior vs posterior regions. **B)** Stereoscope images of organoids after isolation of anterior or posterior region.

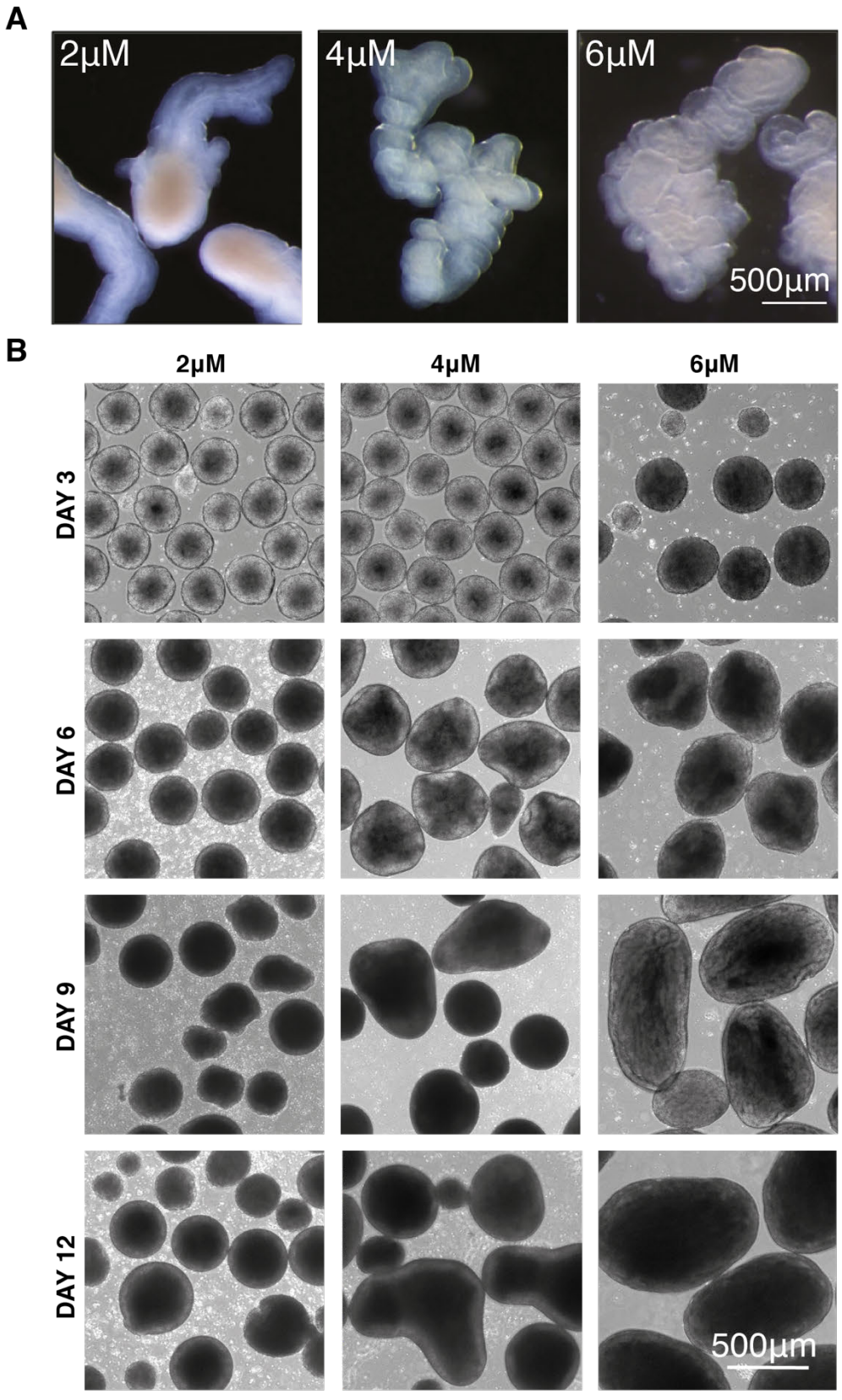

Figure S11: Changes to morphological extensions with increasing Wnt signaling. A) Stereoscope images of WTC organoid morphology with increasing doses of CHIR at day 10 differentiation. **B)** Brightfield images of differentiation time-course conducted in the WTB hiPS cell line.

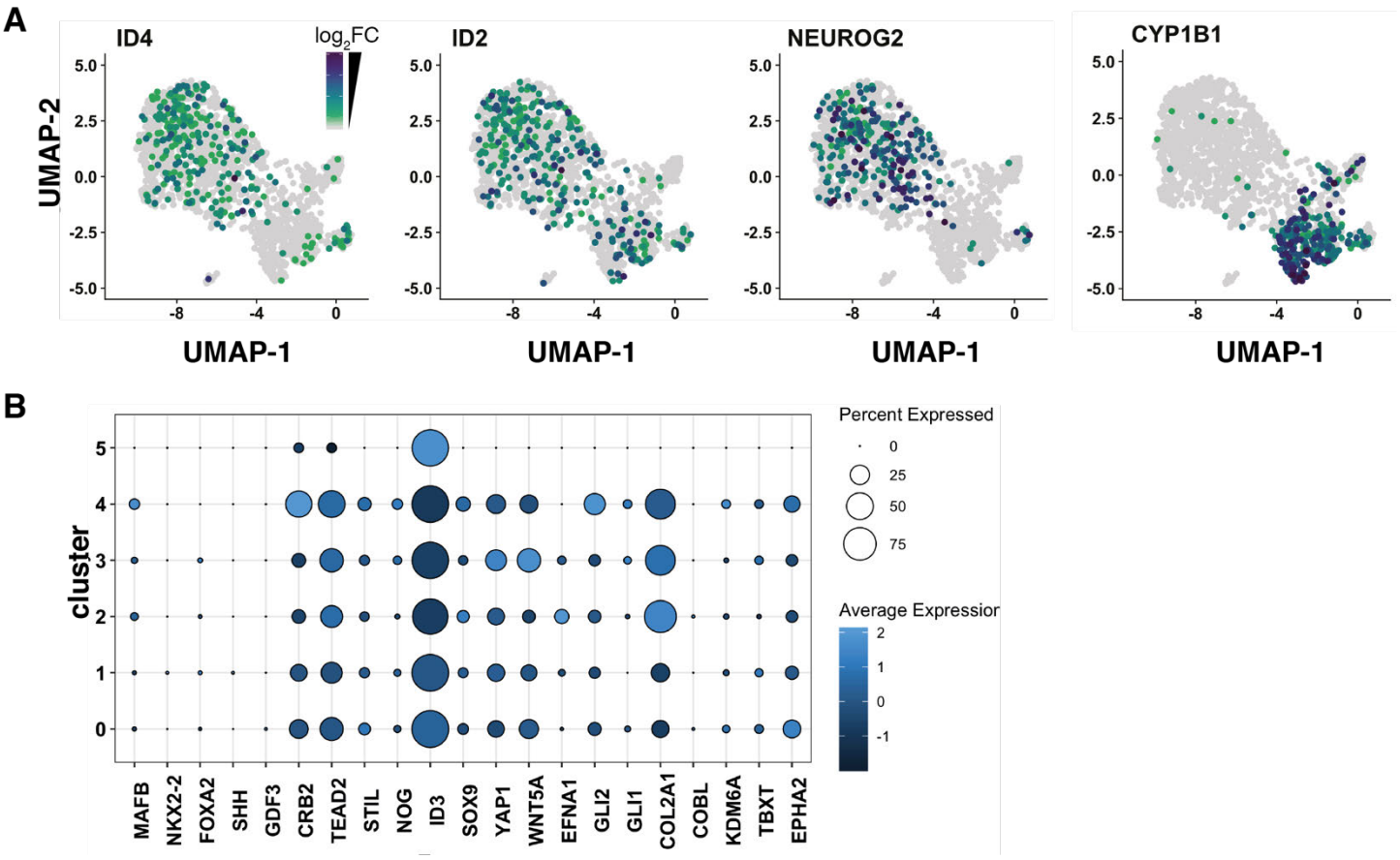

Figure S12: Gene expression within extending and non-extending organoids. A) Panel of genes associated with notochord formation as defined by Gene Ontology and their distribution across clusters of cells. **B)** Gene expression distribution plots associated with BMP signaling (IDs), neuronal lineages (NEUROG2) and presomitic mesoderm (CYP1B1).

Supplementary Movie Legends:

Movie S1: Elongating organoid dynamics. Movie of an example elongating organoid cultured in a 96-well plate, taken over the course of differentiation from day 5 to day 7 with time steps every 20 minutes.

Movie S2: Non-elongating organoid dynamics. Movie of an example non-elongating organoid cultured in a 96-well plate, taken over the course of differentiation from day 5 to day 7 with time steps every 20 minutes.

Movie S3: TBXT and SOX2 location in non-elongating organoid. Movie of a 3D rendered light-sheet image of an example non-elongating organoid stained for TBXT (yellow) and SOX2 (red).

Movie S4: TBXT and SOX2 location in elongating organoid. Movie of a 3D rendered light-sheet image of an example elongating organoid stained for TBXT (yellow) and SOX2 (red).

Movie S5: COL IV and ZO1 location in non-elongating organoid. Movie of a 3D rendered light-sheet image of an example non-elongating organoid stained for COL IV (yellow), ZO1 (red), and DAPI (blue).

Movie S6: COL IV and ZO1 location in elongating organoid. Movie of a 3D rendered light-sheet image of an example elongating organoid stained for COL IV (yellow), ZO1 (red), and DAPI (blue).

Movie S7: β III tubulin and Nestin location in non-elongating organoid. Movie of a 3D rendered light-sheet image of an example non-elongating organoid stained for β III tubulin (TUBB; yellow) and Nestin (red).

Movie S8: β III tubulin and Nestin location in elongating organoid. Movie of a 3D rendered light-sheet image of an example elongating organoid stained for β III tubulin (TUBB; yellow) and Nestin (red).

Supplementary Tables:

Table S1: qPCR Primers

Gene Name (Symbol)	Forward Primer	Reverse Primer
RNA, 18S Ribosomal 5 (RNA18S5, 18S)	CTTCCACAGGAGGCCTACA	CTTCGGCCCACACCCTTAAT
Snail (SNAI1)	TAGCGAGTGGTTCTTCTGCG	GCCAGTCCAAGTCTTCTCGG
Brachyury (TBXT)	TTTCCAGATGGTGAGAGCCG	CCGATGCCTCAACTCTCCAG
SRY-box 2 (SOX2)	AAC CAG CGC ATG GAC AGT TA	CGA GCT GGT CAT GGA GTT GT
NK1 Homeobox 2 (NKX1.2)	CCCTCCCACCACAAGATTTCT	GACCTCCGCCAAACTTTTCCT
T-Box 6 (TBX6)	CATCCACGAGAATTGTACCCG	AGCAATCCAGTTTAGGGGTGT
RNA Binding Fox-1 Homolog 3 (RBFOX3, NEUN)	ACGATCGTAGAGGGACGGAA	AATTCAGGCCCGTAGACTGC
Paired Box 6 (PAX6)	GAGCGAGCGGTGCATTTG	TCAGATTCCTATGCTGATTGGTGAT
Motor Neuron And Pancreas Homeobox 1 (MNX1, HB9)	TCTCTTAACGGGAAGGGGCA	CTAATTCAGGGCGCTCTCGG
LIM Homeobox 2 (LHX2)	AAGTTCAGGCGCAACCTCTT	AAGACGGACGTCACAGTTGG
LIM Homeobox 5 (LHX5)	GTGCAAAGACGACTACCTGAG	CGGTCCGTACAGGATGACAC
Engrailed Homeobox 1 (EN1)	CGCCCAGTTTCGTTTTCGTT	GCAGAACAGACAGACCGACA
Visual System Homeobox 2 (VSX2, CHX10)	CGGCGACACAGGACAATCTT	CCTGTATCCTGTCTTCCGGC
Oligodendrocyte Transcription Factor 2 (OLIG2)	CGCATCCAGATTTTCGGGTC	AAAAGGTCATCGGGCTCTGG
Hes Family BHLH Transcription Factor 1 (HES1)	TCAACACGACACCGGATAAAC	GCCGCGAGCTATCTTTCTTCA
Chordin (CHRD)	TATGCCTTGGACGAGACGTG	ATGTTCTTGCAGCTGACCCT
Noggin (NOG)	GCTGCGGAGGAAGTTACAGA	ACGAGCGCTTACTGAAGCAG
Caudal type homeobox 2 (CDX2)	GCA GCC AAG TGA AAA CCA GG	GCA GCC AAG TGA AAA CCA GG
Mix paired-like homeobox (MIXL1)	TTT TCT CCC CTC TTC CAG GTA T	GGG CAG GCA GTT CAC ATC TA
Aldehyde dehydrogenase 1 family member A2 (ALDH1A2)	TGG ACC AGT GCA GCA AAT CA	ACG CCA TAG CAA TTC ACC CA
Hes family bHLH transcription factor 7 (HES7)	CGGGATCGAGCTGAGAATAGG	GCGAACTCCAATATCTCCGCTT
Wnt family member 3 (WNT3)	CAC AAC ACG AGG ACG GAG AA	GCT TCC CAT GAG ACT TCG CT
Wnt family member 5A (WNT5A)	TCT GGC TCC ACT TGT TGC TC	CGA CCA CCA AGA ATT GGC TTC
Cytochrome P450 family 1 subfamily B member 1 (CYP1B1)	AAGTTCTTGAGGCACTGCGAA	GGCCGGTACGTTCTCCAAAT
Fibroblast growth factor 9 (FGF9)	CCG CTC GCC ACC CGT T	TCTGCAGACATCAGCATGAATCC
Nestin (NES)	CCA CCC TGC AAA GGG AAT CT	GGT GAG CTT GGG CAC AAA AG
Mesenchyme homeobox 1 (MEOX1)	GGC AGC GTA CCC TGA CTT C	GGT CCC CAT TTC CTT GGA ACC
Fibroblast growth factor 8 (FGF8)	GCGCATCCCTAGTGAAGGAG	CCGTCTCCACGATGAGCTTT
Homeobox A2 (HOXA2)	TTT CTC TGA GGG GGC TCC AA	AGT GTC GAG TGT GAA AGC GT
Homeobox B4 (HOXB4)	TACCCCTGGATGCGCAAAGTTC	TGG TGT TGG GCA ACT TGT GG
Homeobox C6 (HOXC6)	GAATGAGGGAAGACGAGAAAGAG	CAT AGG CGG TGG AAT TGA GG
Homeobox B7 (HOXB7)	CGG CGC ATG AAG TGG AAA AA	TCC TGA TTC AGT TCC CAG AGC
Homeobox B9 (HOXB9)	CCG TCT ACC ACC CTT ACA TCC	CGT AGC CGG GTC TTT GAT TAG

Homeobox C10 (HOXC10)	TCG TTC CTT CCT TGC TGC AT	TCT TAG AGC GAC TGG GAG GT

Table S2: CRISPRi guides

Gene Target (Symbol)	Guide sequence
Noggin (NOG)	CTCCTCTCCCGGGTCTACTG
Chordin (CHRD)	AAGGAGCCGCTGCCCGTTCG

Table S3: Antibodies

Gene Target (Symbol)	Species	Company (cat. #)	Dilution
SRY-box 2 (SOX2)	mouse	Abcam (ab79351)	1:200
Paired Box 6 (PAX6)	rabbit	ThermoFisher Scientific (42-6600)	1:200
Brachyury (TBXT)	goat	ThermoFisher Scientific (PA5-46984)	1:400, 1:300
Nestin (NES)	mouse	Santa Cruz (SC-23927)	1:400, 1:200
Hoescht DNA stain	NA	ThermoFisher Scientific (62249)	1:10000
Tubulin Beta 3 Class III (TUBB3/TUJ1)	rabbit	Biolegend (802001)	1:500
N-cadherin (CDH2)	rabbit	Abcam (ab76057)	1:400
Collagen type IV	goat	EMD Millipore (AB769)	1:75
Tight junction protein ZO-1 (TJP1/ZO1)	Mouse	Invitrogen (33-9100)	1:200

Table S4: RNAscope Probes

Gene Target (Symbol)	channel
HOXB1	C2
HOXC6	C1
HOXB9	C3